Ambient vibration measurement-aided multi-1D CNNs ensemble for damage localization framework
demonstration on a large-scale RC pedestrian bridge

Zhou, Yujue; Liu, Yongcheng; Lian, Yuezong; Pan, Tanbo; Zheng, Yonglai; Zhou, Yubao

DOI
10.1016/j.ymssp.2024.111937

Publication date
2024

Document Version
Final published version

Published in
Mechanical Systems and Signal Processing

Mechanical Systems and Signal Processing 224 (2025) 111937

Contents lists available at ScienceDirect

Mechanical Systems and Signal Processing

journal homepage: www.elsevier.com/locate/ymssp

Ambient vibration measurement-aided multi-1D CNNs ensemble for damage localization framework: demonstration on a large-scale RC pedestrian bridge

Yujue Zhou [a], Yongcheng Liu [b,*], Yuezong Lian [a], Tanbo Pan [b], Yonglai Zheng [b], Yubao Zhou [c]

[a] Department of Civil Engineering, Sanming University, Sanming 365004, PR China
[b] Department of Hydraulic Engineering, Civil Engineering College, Tongji University, Shanghai 200092, PR China
[c] Faculty of Civil Engineering and Geosciences, Delft University of Technology, Delft 2600AA, Netherlands

ARTICLE INFO

Communicated by Wei-Xin Ren

Keywords:
Pedestrian bridge
Pile foundations
Finite element modelling
Ambient vibration measurement
Structural damage detection
1D convolutional neural networks

ABSTRACT

Damage localization in civil infrastructure, such as large-scale reinforced concrete (RC) pedestrian bridges, is essential for conducting precise maintenance and avoiding catastrophic failures. In this study, multiple one-dimensional convolutional neural networks (1-D CNNs) are developed for automatically extracting implicit damage-sensitive features from the structural raw dynamic responses to localize damage in the pile foundations of pedestrian bridges considering uncertainties such as environmental and operational variations (EOVs) inherent in dynamic responses. For this purpose, transient dynamics numerical computation models are established to simulate the multi-point dynamic response of the structure under different typical damage scenarios, forming the baseline dataset. Then, on-site vibration tests are conducted on the structural prototype. Ambient vibrations of the real intact bridge are considered EOVs and integrated into the baseline dataset, forming the test dataset. Additionally, the intact structural dynamic response with measured EOVs replaces the simulated intact structural dynamic response in the baseline dataset to form a reference dataset. The network architectures based on one-dimensional convolutional layers proposed in this paper are trained on the baseline dataset and reference datasets to obtain baseline and reference models. Subsequently, model performance evaluation is conducted on the test dataset, and the results indicate a significant decrease in the performance of damage models based on a single deep learning when EOVs are present. However, integrating the baseline and reference models achieves zero false negative/positive predictions which is safety-oriented and an exemplary classification accuracy of up to 97.2 %.

1. Introduction

Pedestrian bridges, designed to facilitate pedestrian-vehicle diversion and ensure convenient passage, are extensively integrated into global urban transportation systems. As large-scale complex spatial structural systems, these bridges are typically formed by an upper girder-slab structure closely connected to the lower pile foundations through bridge piers. Whereas during the operational

* Corresponding author.
E-mail address: yongcheng.liu@kuleuven.be (Y. Liu).

https://doi.org/10.1016/j.ymssp.2024.111937
Received 8 January 2024; Received in revised form 2 September 2024; Accepted 8 September 2024
Available online 25 September 2024

lifespan, pile foundations are prone to structural damage resulting from slope deformations, uneven settlement, and potential seismic activities [1,2]. Moreover, the corrosion of internal steel bars within the pile foundations as they traverse diverse engineering media [3], coupled with the development of loading-induced plastic hinge regions, results in a decreased global stiffness of structural members, which ultimately jeopardizes the overall safety of pedestrian bridges. Notably, pile foundations are usually constructed as concealed engineering components, making it challenging to localize damage promptly through conventional routine inspections. Therefore, establishing a real-time damage localization framework for the pile foundations of large pedestrian bridges holds significant engineering value [4].

Vibration-based structural damage detection (VSDD) methods [5,6], as one of the current mainstream Structural Health Monitoring (SHM) techniques [7,8], operate on the principle that structural damage can be identified and quantified by analyzing changes in the structure's dynamic properties pre- and post-damage occurrence [9]. Numerous studies focusing on VSDD methods have been conducted [10–14], broadly, which can be summarized into two major categories: parametric and nonparametric methods. Parametric methods [15–17] utilize alterations in the dynamic parameters as indicators of the formation, location, and severity of structural damage [18–21]. Despite the prevalent utilization, certain constraints endure as follows: (i) Subtle changes in dynamic properties induced by local early-stage damage are only observable in higher-order modes, which are formidable to excite in the context of large-scale structures; (ii) Various hand-crafted parameters, dependent on substantial expert knowledge while constrained to certain structural types and necessitate stringent sensor placement, often exhibits poor applicability in complex and diverse structures; (iii) The sensitivity of specific parameters extends beyond damage to encompass external influences, including ambient noise and temperature variations. On the other hand, nonparametric methods, fundamentally entailing the application of anomaly detection algorithms, aim to extract damage-sensitive features directly from measured signals [22–24], e.g., using time series modelling and statistical classification. Similarly, the main drawbacks of these approaches are summarized as (i) The environmental and operational variations (EOVs) contained in dynamic responses of large-scale infrastructures far exceed that of steady-state operation of mechanical systems, those non-damage-related influences would significantly impede the efficacy of such methods; (ii) The need for high computational complexity and an extensive number of sampling points poses challenges for real-time monitoring.

In light of the rapid evolution of computer hardware, which facilitates large-scale parallel computing, machine learning (ML) and deep learning (DL) are introduced into SHM and have attained broad recognition [10,25,26]. In the early implementation of ML-based VSDD methods, a prevalent paradigm was followed: non-linear mapping relationships between manually crafted damage-sensitive features and structural states were typically established using shallow algorithms such as decision trees [27], support vector machines [28], and multi-layer perceptron [29,30]. This approach demonstrated significant effectiveness in scenarios characterized by limited data and relatively straightforward tasks [31]. Nonetheless, the excellent performance critically hinges on the selection of suitable damage-sensitive features as well as the classifiers. Additionally, it cannot be guaranteed that a particular feature/classifier set represents the optimal choice for all instances of structural damage scenarios [32]. On the other hand, the DL-based VSDD methods are characterized by their outstanding automatic feature extraction [33], attributed to the utilization of deep artificial neural networks in place of the shallow algorithms in ML. With the increase in hidden layers, the non-linear statistical modelling capacity of DL significantly improves, endowing it with the capability to handle complex patterns and objects in very large datasets. It is worth noting that, due to the escalating number of training parameters in DL algorithms, overfitting is prone to occur in scenarios with small sample sizes, leading to a degradation of the generalization ability in such damage recognition models. During this period, ML-based and DL-based VSDD models have achieved positive achievements for small-scale infrastructures or simple industrial mechanical systems. But in the realm of large-scale complex civil structures, where the variety and complexity of damage scenarios are more pronounced, the construction or extraction of effective damage-sensitive features proves to be a formidable challenge.

Over the past decade, Convolutional Neural Networks (CNNs) and their variants have gained notable successes in numerous domains, e.g., face recognition [34,35], and behaviour detection [36,37], attributing to the remarkable ability to automatically extract implicitly hierarchical features with spatial invariance from raw data and the outstanding adaptability and model generalization [38]. Compared to the above models using fully connected layers, which completely lose spatial resolution during the statistical modelling process, CNNs have an inherent advantage in addressing VSDD tasks considering the spatial correlations of measurement at different points in the same moment could be well captured [39–42]. Yet, solely relying on such spatial correlations of dynamic responses makes it challenging to achieve the real-time localization target, in view of the structural health state is actually a time-dependent attribute providing insights of changes in physical properties related to damage. Hence, 1D CNNs entailing both spatial and temporal resolution with a more compact structure have gained great attention recently.

A series of studies reported by Avci and Abdeljaber et al. focused on the 1D CNNs-based real-time VSDD method via raw acceleration signals from large-scale experiments conducted on a grandstand simulator [43], with an application on wireless sensor networks [44], and an enhanced version requiring only two measurement sets [45], these research highlighted the practical value of such approach when applied to complex structures. Moreover, Zhou et al. first adopted a hybrid methodology for VSDD on typical high-pile wharfs [46]. The results indicated the superior performance of the 1D CNNs in detecting structural damage directly from raw displacement response data. Notably, traditional 2D CNNs can achieve spatial and temporal resolution simultaneously through data reconstruction, but this introduces more parameters, leading to escalating overfitting risks and computational demands.

Currently, the primary emphasis of research on 1D CNNs-based VSDD for large-scale infrastructures lies in verifying the feasibility/accuracy of their methodologies/algorithms [43,45–51]. Given the vast number of potential damage scenarios in large-scale structures and the challenges associated with obtaining comprehensive real-world measurement, employing dynamic responses generated through numerical simulations under various damaged scenarios for training data has become a prevailing approach. However, it is crucial to recognize that uncertainties inherent in real-world monitoring data can substantially affect the robustness of the aforementioned VSDD models. While some related studies have considered these uncertainties [52–55], it is noted that the EOVs addressed are artificially generated, typically using white noise signals. In-depth investigations into the model's performance and robustness in the presence of real ambient noises and actual EOVs remain limited and warrant further exploration [23,56]. Indeed, the decline in performance of such models under high-level EOVs, which are common issues in actual engineering scenarios, is inevitable. The more severe impact is the increased false-negative rate of predictions. In other words, the model may potentially misclassify a damaged state as intact, and persisting in such 'trust' in the worst-case scenario could lead to catastrophic accidents, which should be strongly avoided. This study presents an ambient vibration measurement-aided damage localization framework in the manner of a multi-1D CNNs ensemble for a large-scale Reinforced Concrete (RC) pedestrian bridge considering EOVs, which realizes exceptional safety-oriented damage identification and provides enhanced performance of damage localization. The proposed methodology fuses simulated acceleration responses from various Finite Element (FE) models with on-site ambient vibration measurement from an intact structural prototype. The essence of this framework lies in its two-stage multi-model ensemble procedure. The first stage aims to eliminate false negative/positive predictions, and the second stage enhances the localization performance for different damage scenarios. This approach provides novel insights into how fusion data can be better utilized for improving methodology performance considering the factor of EOVs.

The paper is organized as follows. In Section 2, the significance and objectives of this study will be conveyed. In Section 3, the workflow of the complete framework is presented with a formalized description. In Section 4, the simulation process of the RC pedestrian bridge is further demonstrated, and the simulated acceleration response of different damage models and the on-site ambient vibration measurements are both obtained. A concise description of the overall architecture and specific parameters of the established 1D CNNs is given in Section 5. Section 6 reveals the post-processing of the simulated and measured data and the training and validation of 1D CNNs. In Section 7, the performance of baseline and reference models on different datasets are evaluated, and the novel multi-model ensemble strategy for damage localization is proposed based on excellent results. Finally, conclusions are gathered in Section 8.

2. Research significance and objectives

Large pedestrian bridges often cross traffic arteries and are simultaneously subjected to various dynamic and environmental factors, including pedestrian loads, heavy vehicles passing under the bridge, and temperature changes. Consequently, their dynamic responses contain a large amount of EOVs. Current damage identification/localization methods based on structural dynamic responses within DL frameworks experience significant efficiency degradation when dealing with high-level EOVs. Therefore, introducing a one-dimensional convolutional neural network with the ability to automatically construct features with time and space translation invariance into the damage localization of the pile foundation in large pedestrian bridge structures holds broad application prospects.

This study aims to achieve the following two objectives: (i) Establish an intelligent damage localization method framework for large pedestrian bridge pile foundations using one-dimensional convolutional neural networks that integrate finite element simulation dynamic responses and on-site measured ambient vibration responses of a structural prototype; (ii) Explore a safety-oriented damage localization strategy for the pile foundations of large-scale RC pedestrian bridges based on the idea of multi-model ensemble.

3. Methodology

The presented framework aims to empower 1D CNNs-based damage localization models, developed within the data-driven vibration-based structural health monitoring strategy, to deliver safety-oriented, enhanced-performance results for a RC pedestrian bridge. The comprehensive framework is delineated in six steps:

(i) Selection of damage scenarios that have a high likelihood for the monitored structure. This can be achieved by traditional methods like structural fragility analysis. For simplicity, we consider specific reductions in overall stiffness at various pile foundations as typical damage scenarios in this research.
(ii) Construction of numerical models for all chosen damage scenarios. The accuracy of these models is further corroborated by comparing the dynamic characteristics between the prototype structure and the numerical model of the undamaged state.
(iii) Execution of transient dynamic calculations for all scenarios, where the excitation is an impact unloading. The multi-point dynamic responses for all scenarios are recorded and labelled synchronously with the corresponding damage scenario number, forming the baseline dataset.
(iv) Measurement of the on-situ vibration responses of the structure (in this study, the freshly inspected pedestrian bridge can be considered an intact structure) under ambient excitation. The sensor layout corresponds with the locations of the sampling points in step (iii).
(v) Construction of various datasets, including a simulated dataset and a fusion dataset. The simulated responses at corresponding points of the numerical model for all damage scenarios form the simulated dataset. EOVs processed by on-site vibration measurements are added to the relevant part of the simulated dataset to create the fusion dataset, which mimics more realistic vibration responses.
(vi) Execution of damage detection tasks using 1D CNNs models trained on different datasets. The baseline models are trained on the simulated dataset without samples of the intact scenario, while the reference model is trained on the fusion dataset. This two-stage robust strategy employing both baseline and reference models yields safety-focused, superior-performance results for damage detection.

The six steps described above will be formalized more specifically in the remainder of this section.

Consider a structure equipped with a total of $\boldsymbol{n}$ acceleration sensors that record the multi-point vibration responses. Once a total of $\boldsymbol{m}$ damaged scenarios (including the scenario of the structure is intact) are determined as follows:

$$\mathbb{D}_s = \{I_0, D_1, D_2, \cdots D_{m-1}\} \tag{1}$$

Where $\mathbb{D}_s$ denote the set of selected damage scenarios. The term I_0 and D_i represent the structural intact state and damaged scenarios with overall stiffness decay at structural components with serial number $i^{\#}$ respectively.

The first 3 mode shapes and modal frequencies of prototype structure in its intact state (or reference state) and the corresponding numerical model (scenario of I_0) could be obtained by in-situ vibration testing and calculation of structural transient dynamics respectively, and represented as:

$$\Phi_p = [\ \varphi_p^{(1)},\ \ \varphi_p^{(2)},\ \ \varphi_p^{(3)}\ ] \tag{2}$$

$$\Phi_{NM} = [\ \varphi_{NM}^{(1)},\ \ \varphi_{NM}^{(2)},\ \ \varphi_{NM}^{(3)}\ ] \tag{3}$$

$$F_p = [\ f_p^{(1)},\ \ f_p^{(2)},\ \ f_p^{(3)}\ ] \tag{4}$$

$$F_{NM} = [\ f_{NM}^{(1)},\ \ f_{NM}^{(2)},\ \ f_{NM}^{(3)}\ ] \tag{5}$$

where Φ_p, F_p and Φ_{NM}, F_{NM} denote the first three mode shapes and modal frequencies of the prototype structure and corresponding numerical model of intact monitored structure respectively. While the terms $\varphi_p^{(i)}$,$\varphi_{NM}^{(i)}$ and $f_p^{(i)}$, $f_{NM}^{(i)}$ represent the $\boldsymbol{ith}$-order mode shapes and natural frequency of prototype structure and corresponding numerical model of intact monitored structure respectively. It should be noted that there is a one-to-one correspondence between the structural prototype and the sampling points of the dynamic response of the corresponding numerical model.

Establishing a data-driven damage detection model in VSDD framework requires consistency between the structural dynamic characteristics of the structural prototype and the corresponding numerical model. Based on the final damage identification results, it is argued that the computational results of the numerical model are sufficient to train an efficient damage identification model by imposing the following restrictions on the first three orders of mode shapes and modal frequencies of the structural prototype and the corresponding numerical model:

$$\Phi_p \sim \Phi_{NM} \tag{6}$$

where the symbol '$\sim$' represents the similarity operator, which means only the consistency of general morphological characteristics of mode shapes between the prototype structure and the numerical model was required. For example, if the prototype structure's first three mode shapes are lateral, longitudinal and plane torsional mode, the numerical model's corresponding mode shapes were required to be the same.

$$\begin{cases} D(F_{NM}\ F_p) = \sqrt[p]{\left|f_{NM}^{(1)} - f_p^{(1)}\right|^p + \left|f_{NM}^{(2)} - f_p^{(2)}\right|^p + \left|f_{NM}^{(3)} - f_p^{(3)}\right|^p} \\ D(F_{NM}\ F_p) < \epsilon \end{cases} \tag{7}$$

where $D(F_{NM}\ F_p)$ represents the Minkowski distance between the first three modal frequencies vector of the prototype structure and its numerical model. It should be noted that multiple influence factors such as monitoring precision, structural characteristics and hardware facility are required to be considered comprehensively when determining the specific value of tolerance ϵ and parameter p.

Once the appropriate numerical model of the intact structure prototype, namely the benchmark model, which is confirmed by constraints of equations of (6) and (7) has been established, the next step is to build a total of m numerical models for all damaged scenarios $\mathbb{D}_s$ based on that benchmark model.

The raw acceleration time-series calculated by all numerical models could be represented as follows, it should be noted that all transient dynamic simulations use the same excitation scheme.

$$\begin{cases} \boldsymbol{I}_0 = \left[I_0, I_{\Delta t}, I_{2\Delta t}, \cdots, I_{t_0}\right]^T \\ \boldsymbol{D_i} = \left[D_0^{(i)}, D_{\Delta t}^{(i)}, D_{2\Delta t}^{(i)}, \cdots, D_{t_0}^{(i)}\right]^T \end{cases} \tag{8}$$

Where the terms $I_{k\Delta t}$ and $D_{k\Delta t}^{(i)}$ ($0 \le k \le \frac{t_0}{\Delta t} | k \in \mathbb{N}$) represent the calculated multi-point dynamic responses at kth time step at intervals of Δt for the intact scenario and damaged scenario $\boldsymbol{i}^{\#}$, respectively. The subscript t_0 denotes the timespan of transient dynamic computation.

Assuming that each calculated single-point dynamic response at the sampling point $\boldsymbol{s}^{\#}$ ($\mathbf{s} \le n | \mathbf{s} \in \mathbb{N}$) consists of n_l frames ($n_l = t_0/\Delta t$), the next step is to align $\boldsymbol{n}$ single-point dynamic responses acquired at a total of n sampling points in time steps as follows:

$$\boldsymbol{I}_0 = \begin{bmatrix} I_{1,\ 0} & I_{2,\ 0} & \cdots & I_{n,\ 0} \\ I_{1,\ \Delta t} & I_{2,\ \Delta t} & \cdots & I_{n,\ \Delta t} \\ \vdots & \vdots & \ddots & \vdots \\ I_{1,\ t_0} & I_{2,\ t_0} & \cdots & I_{n,\ t_0} \end{bmatrix}_{n_l \times n} \qquad \boldsymbol{D_i} = \begin{bmatrix} D^{(i)}_{1,0} & D^{(i)}_{2,0} & \cdots & D^{(i)}_{n,0} \\ D^{(i)}_{1,\Delta t} & D^{(i)}_{2,\Delta t} & \cdots & D^{(i)}_{n,\Delta t} \\ \vdots & \vdots & \ddots & \vdots \\ D^{(i)}_{1,t_0} & D^{(i)}_{2,t_0} & \cdots & D^{(i)}_{n,t_0} \end{bmatrix}_{n_l \times n} \tag{9}$$

where the term $I_{i,j} \in \boldsymbol{I}_0$ $(0 \le i \le n, 0 \le j \le n_l | i,j \in \mathbb{N})$ represent the output acceleration of the sampling point $\boldsymbol{i}^{\#}$ at time step $\boldsymbol{j}^{\#}$ for the intact scenario. While the term $D^{(i)}_{j,k} \in \boldsymbol{D_i}$ $(0 \le i < m, 0 \le j \le n, 0 \le k \le n_l | i,j,k \in \mathbb{N})$ is the output acceleration of the sampling point $\boldsymbol{j}^{\#}$ at time step $\boldsymbol{k}^{\#}$ for the damaged scenario $\boldsymbol{i}^{\#}$.

In the field vibration test, the acceleration response under environmental excitation recorded at a total of $\boldsymbol{n}$ sampling points can be expressed as follows:

$$\boldsymbol{V_a} = \begin{bmatrix} v_{1,\ 0} & v_{2,\ 0} & \cdots & v_{n,\ 0} \\ v_{1,\ \Delta T} & v_{2,\ \Delta T} & \cdots & v_{n,\ \Delta T} \\ \vdots & \vdots & \ddots & \vdots \\ v_{1,\ T_0} & v_{2,\ T_0} & \cdots & v_{n,\ T_0} \end{bmatrix}_{q \times n} \tag{10}$$

where the term $v_{i,j} \in \boldsymbol{V_a}$ $(0 \le i \le n, 0 \le j \le n_l | i,j \in \mathbb{N})$ represent the recorded acceleration of the sampling point $\boldsymbol{i}^{\#}$ point at time step $\boldsymbol{j}^{\#}$ of the structural prototype in its current state (in this study, the structural current state is equivalent to the intact state). The first subscript of each element of the matrix $\boldsymbol{V_a}$ denotes the sampling point serial number, and ΔT in the second subscript denotes the sampling interval of the acceleration acquisition system. The sampling interval ΔT should be selected according to the field conditions and the analysis accuracy and is not required to be equal to the calculation time step of the numerical model. The first dimension q of the matrix $\boldsymbol{V_a}$ represents the total amount of data at the test duration T_0 and sampling interval ΔT.

Considering that the test duration and sampling interval of the field vibration test are different from the corresponding values in the numerical model calculation, the field vibration test data must be cropped. Given a random integer $\boldsymbol{i}$ between 0 and $\left(\frac{T_0}{\Delta T} - \frac{t_0}{\Delta T}\right)$, with $\boldsymbol{i}$ as the starting point, a submatrix containing $\frac{t_0}{\Delta T}$ rows is sequentially intercepted in the matrix $\boldsymbol{V_a}$. The new matrix formed by resampling this submatrix at $\frac{\Delta t}{\Delta T}$ row intervals is represented as follows:

$$V_a' = \begin{bmatrix} v_{1,\ i^*\Delta t} & v_{2,\ i^*\Delta t} & \cdots & v_{n,\ i^*\Delta t} \\ v_{1,\ 2i^*\Delta t} & v_{2,2\ i^*\Delta t} & \cdots & v_{n,\ i^*\Delta t} \\ \vdots & \vdots & \ddots & \vdots \\ v_{1,\ n_l^*\Delta t} & v_{2,\ n_l^*\Delta t} & \cdots & v_{n,\ n_l^*\Delta t} \end{bmatrix}_{n_l \times n} \tag{11}$$

The next step is to construct the dataset needed to train the 1D CNNs-based damage detection model. The calculated response of the numerical model when the structure is in the intact state and the measured dynamic response in the field is element-wise summed to obtain a new dataset ($\boldsymbol{V_s}$) for simulating the dynamic response of the structural prototype under real operating conditions.

$$[\boldsymbol{V_s}] = [\boldsymbol{I}_0] + [\boldsymbol{V}_a'] \tag{12}$$

Each time slice of the dynamic response of all sampling points in $\boldsymbol{I}_0$, $\boldsymbol{D_i}$ and $\boldsymbol{V}_a^*$ is labelled by the corresponding scenario serial number. For example, in the damaged scenario $\boldsymbol{i}^{\#}$, total n_l rows $\in \boldsymbol{D_i}$ are labelled as category $\boldsymbol{i}$. All labelled data and labels themselves would then be normalized in intervals $(-1, 1)$ and one-hot encoded, respectively. The manipulated labelled data could be represented as follows:

$$I_0^* = \begin{bmatrix} NI_{1,\ 0} & NI_{2,\ 0} & \cdots & NI_{n,\ 0} & 1_{Column\ (n+1)} & 0 & \cdots & 0_{Column\ (n+m)} \\ NI_{1,\ \Delta t} & NI_{2,\ \Delta t} & \cdots & NI_{n,\ \Delta t} & 1_{Column\ (n+1)} & 0 & \cdots & 0_{Column\ (n+m)}\ 1 \\ \vdots & \vdots & \ddots & \vdots & & & \ddots & \\ NI_{1,\ t_0} & NI_{2,\ t_0} & \cdots & NI_{n,\ t_0} & 1_{Column\ (n+1)} & 0 & \cdots & 0_{Column\ (n+m)} \end{bmatrix}_{n_l \times (n+m)} \tag{13}$$

$$D_i^* = \begin{bmatrix} ND^{(i)}_{1,0} & ND^{(i)}_{2,0} & \cdots & ND^{(i)}_{n,0} & 0_{Column(n+i)} & \cdots & 1_{Column(n+i)} & \cdots & 0_{Column(n+m)} \\ ND^{(i)}_{1,\Delta t} & ND^{(i)}_{2,\Delta t} & \cdots & ND^{(i)}_{n,\Delta t} & 0_{Column(n+i)} & \cdots & 1_{Column(n+i)} & \cdots & 0_{Column(n+m)} \\ \vdots & \vdots & \ddots & \vdots & & & \ddots & & \\ ND^{(i)}_{1,t_0} & ND^{(i)}_{2,t_0} & \cdots & ND^{(i)}_{n,t_0} & 0_{Column(n+i)} & \cdots & 1_{Column(n+i)} & \cdots & 0_{Column(n+m)} \end{bmatrix}_{n_l \times (n+m)} \tag{14}$$

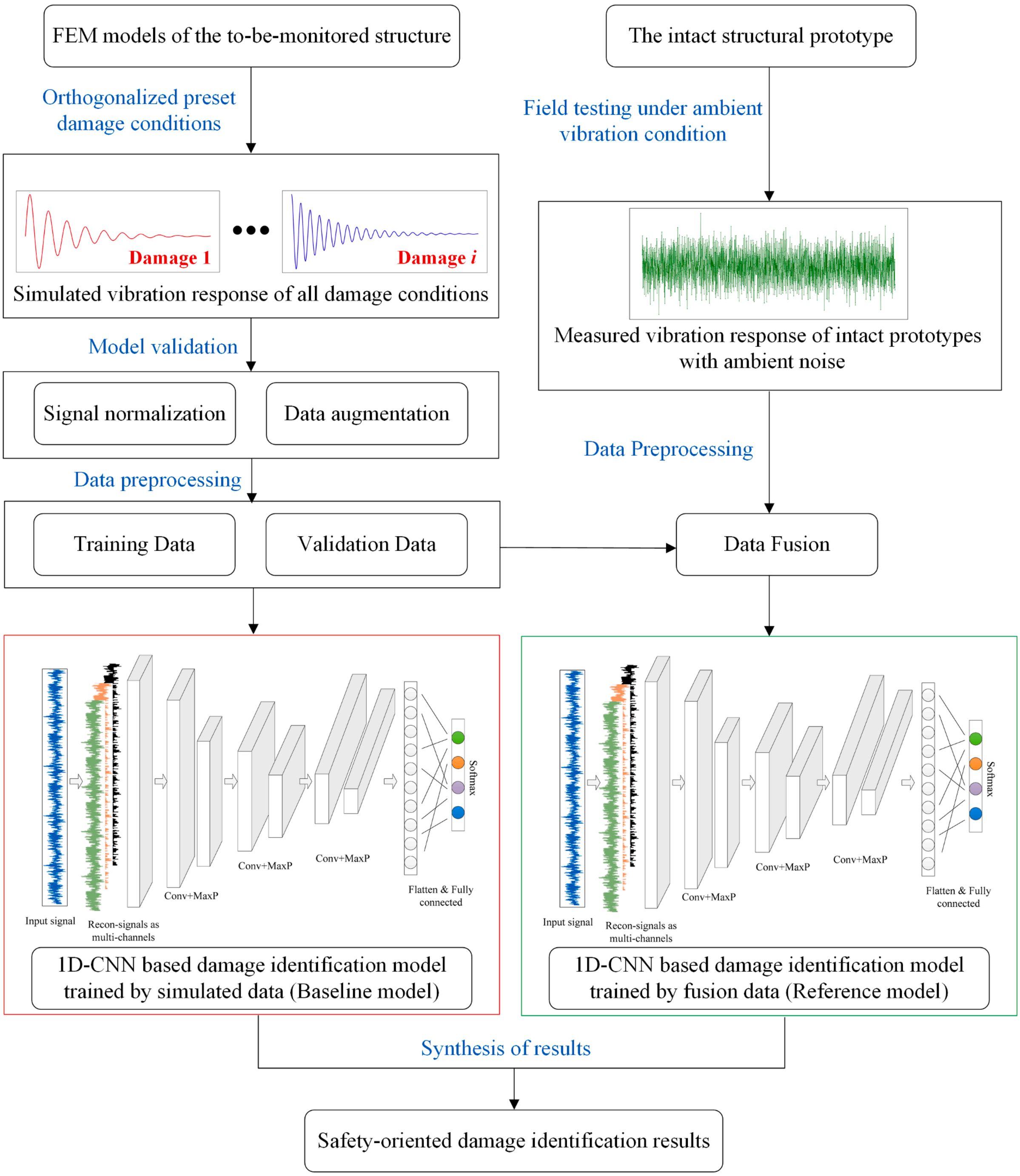

Fig. 1. Workflow of the proposed safety-oriented damage localization framework combining simulated responses and on-site measured ambient vibration responses.

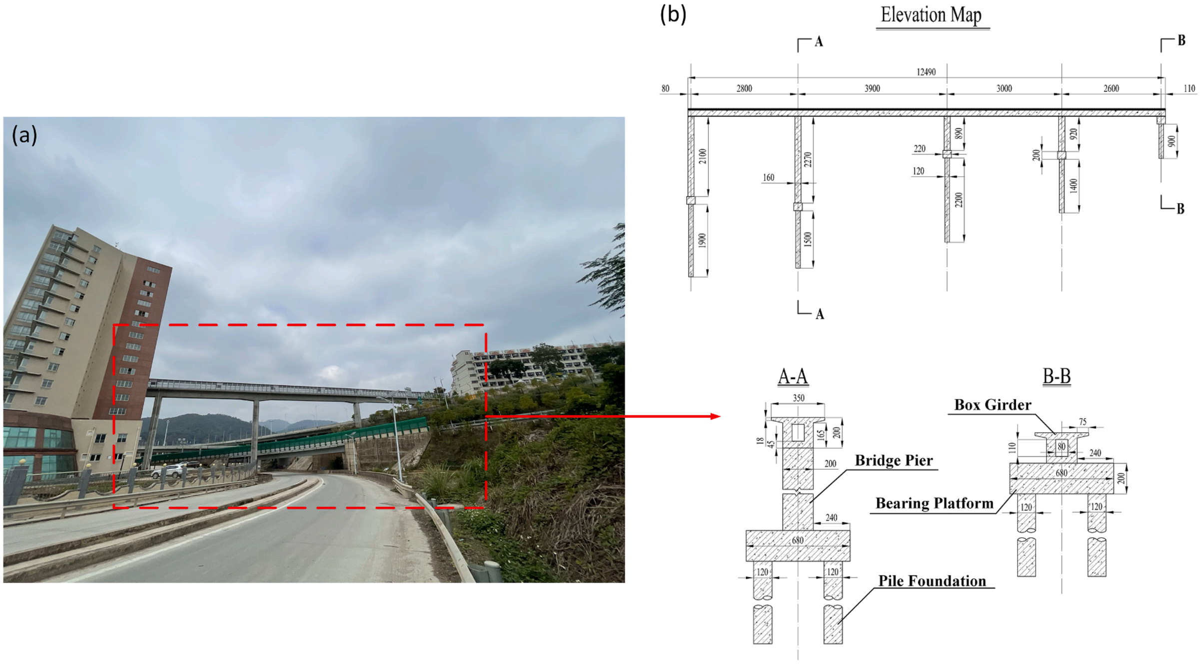

Fig. 2. Geometrical details of the bridge with (a) a site photo and (b) the elevation map with cross-section views.

$$V_s^* = \begin{bmatrix} nv_{1,i^*\Delta t} & nv_{2,i^*\Delta t} & \cdots & nv_{n,i^*\Delta t} & 1_{Column(n+1)} & 1_{Column(n+2)} & \cdots & 0_{Column(n+m)} \\ nv_{1,2i^*\Delta t} & nv_{2,2i^*\Delta t} & \cdots & nv_{n,2i^*\Delta t} & 1_{Column(n+1)} & 1_{Column(n+2)} & \cdots & 0_{Column(n+m)} \\ \vdots & \vdots & \ddots & \vdots & & & \ddots & \\ nv_{1,\, n_l^*\Delta t} & nv_{2,\, n_l^*\Delta t} & \cdots & nv_{n,\, n_l^*\Delta t} & 1_{Column(n+1)} & 1_{Column(n+2)} & \cdots & 0_{Column(n+m)} \end{bmatrix}_{n_l \times (n+m)} \tag{15}$$

Total $m-1$ damaged scenario datasets were spliced with datasets I_0^* and V_s^* along the vertical axis, named baseline and reference dataset ($D_b \& D_r$), respectively. The 1D CNNs-based damage detection models that use these two data sets are referred to as the baseline model and the reference model, respectively.

$$D_b = \begin{bmatrix} I_0^* \\ D_1^* \\ D_i^* \\ D_{m-1}^* \end{bmatrix}_{(n_l^*m)\times(n+m)} \qquad D_r = \begin{bmatrix} V_s^* \\ D_1^* \\ D_i^* \\ D_{m-1}^* \end{bmatrix}_{(n_l^*m)\times(n+m)} \tag{16}$$

In order to comprehensively evaluate the performance of the 1D CNNs-based damage detection model and optimize the model architecture and corresponding hyperparameters, it is necessary to construct a test dataset containing the in-situ recorded ambient vibrations and the results of numerical calculations for all scenarios, so as to simulate the real dynamic response of the Structural prototype under the actual working conditions, and the construction process is as follows:

$$\begin{gathered} D_a = \begin{bmatrix} V_s^* & V_s^* & \cdots & V_s^* \end{bmatrix}^T_{(n_l^*m)\times(n+m)} \\ D_t = D_b + D_a \end{gathered} \tag{17}$$

where D_a represents stacking the matrix (V_s^*) $\boldsymbol{m}$ times along the vertical axis. The matrix D_t is the test dataset that incorporates the numerically calculated dynamic response under the impact load excitation and the ambient vibration under the environmental excitation.

Then, for the above-generated dataset, the Back Propagation (BP) algorithm is used to train the 1D CNNs-based SDD models. Assuming that the baseline and reference models trained based on baseline and reference datasets, respectively, have different accuracies in recognizing different damage scenarios, the final damage recognition results would be output as per the following equation:

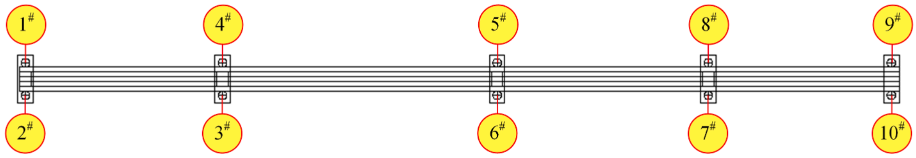

Fig. 3. Pile foundation numbers of the pedestrian bridge from top view.

Table 1
Damage conditions setup.

Damage condition number	Number of pile foundations with reduced stiffness
condition $0^{\#}$	none
condition $i^{\#}$	PF $i^{\#}$

Remark: i in Table 1 represents an integer from 1 to 10, which corresponds to the pile foundation number in Fig. 3.

Table 2
Summary of material parameters for numerical analysis.

Mass density, ρ (kg/m^3)	2600
Elastic modulus of intact components, E_i (GPa)	40
Elastic modulus of damaged components, E_d (GPa)	10
Poisson's ratio, ν	0.2
Damping ratio, ζ	0.05
Mass damping coefficient, α	0.031
Stiffness damping coefficient, β	0.078

$$\begin{cases} res = \omega^* f_{out}^{(b)}(x_i) + (1-\omega)^* f_{out}^{(r)}(x_i) \\ \quad \omega = 1 \quad for \quad f_{out}^{(b)}(x_i) \in \mathscr{H} \\ \quad \omega = 0 \quad for \quad f_{out}^{(r)}(x_i) \in \mathscr{L} \end{cases} \tag{18}$$

where the term x_i represents any input frame of measured dynamic responses. $f_{out}^{(b)}$ and $f_{out}^{(r)}$ represent the discriminant results of baseline and reference models, respectively. The set $\mathscr{H}$ indicates that the baseline model performs more superior in this set of damaged scenarios than the reference model, and set $\mathscr{L}$ has the opposite meaning. The schematic diagram of the suggested methodology can be illustrated in Fig. 1.

4. Case studies

In this section, a continuous beam pedestrian bridge located in Sanming City, Fujian Province was selected as the research object. Firstly, the damage scenarios of the pile foundation were discretized into 10 typical single-pile damaged conditions and the intact condition. Secondly, 11 FE. models for all damaged conditions were established by ANSYS software, respectively. Subsequently, the natural frequencies and mode shapes obtained from the modal analysis will be used to verify the rationality of the pedestrian bridge' FE models. Finally, the acceleration response of the measurement points, computed through transient dynamic calculation, will be leveraged to analyze the impact of global structural damage of the pile foundation on the pedestrian bridge's dynamic response.

4.1. Geometry of the pedestrian bridge

The superstructure of the continuous beam pedestrian bridge is a box girder made of concrete C50, and the substructure consists of 4 bridge piers, 5 bearing platforms, and 10 pile foundations, which are made of concrete C30, concrete C30, and concrete C40, respectively. The box girder is 124.9 m long; the cross-section of bridge piers is 2 m long and 1.6 m wide; the bearing platforms have a uniform size, 6.8 m long, 2.2 m wide, and 2 m high; the radius of pile foundations is 0.6 m. Details about the dimensions of the pedestrian bridge can be found in Fig. 2.

4.2. Structural damage scheme

Structural damage will cause permanent, irreversible changes in physical properties, especially in the distribution of structural stiffness, which can be utilized for damage identification. Predominantly, damage manifests as a reduction in the residual effective

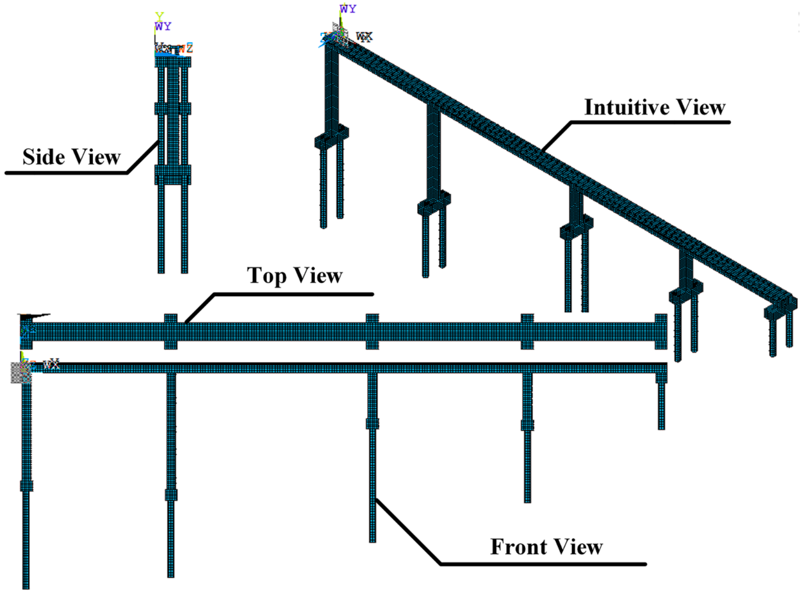

Fig. 4. Finite element model of the pedestrian bridge in different views.

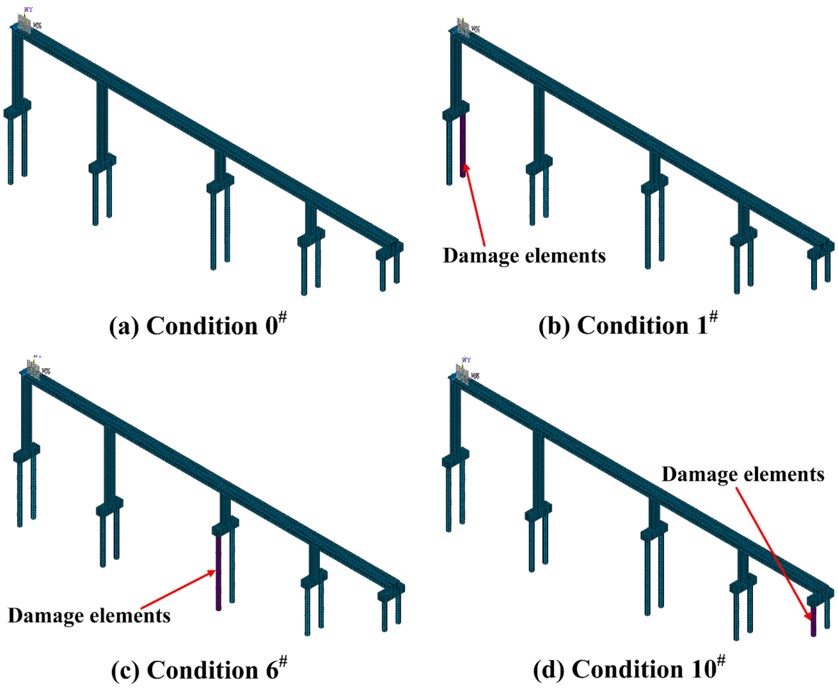

Fig. 5. Several FE models corresponding to different damage conditions, with the purple-colored component indicating a 75 % reduction in stiffness. (For interpretation of the references to colour in this figure legend, the reader is referred to the web version of this article.)

cross-sectional area, corresponding to a decline in structural stiffness. As such, following Saint-Venant's principle, structural damage can be modelled in numerical simulations by decreasing the elastic modulus of specific components. This approach is widely used in the existing literature in the field of SHM [46,57–59].

In this study, the two pile foundations located at the end with a bridge pier (the left end) were set as PF $1^{\#}$ and PF $2^{\#}$, the number of pile foundations increased along the direction of the box girder, PF $9^{\#}$ and PF $10^{\#}$ were both located at the end without a bridge pier (the right end). Other details about the settings were given in Fig. 3.

According to the idea of orthogonal experiments, complex global structural damage scenarios that may exist for pile foundations

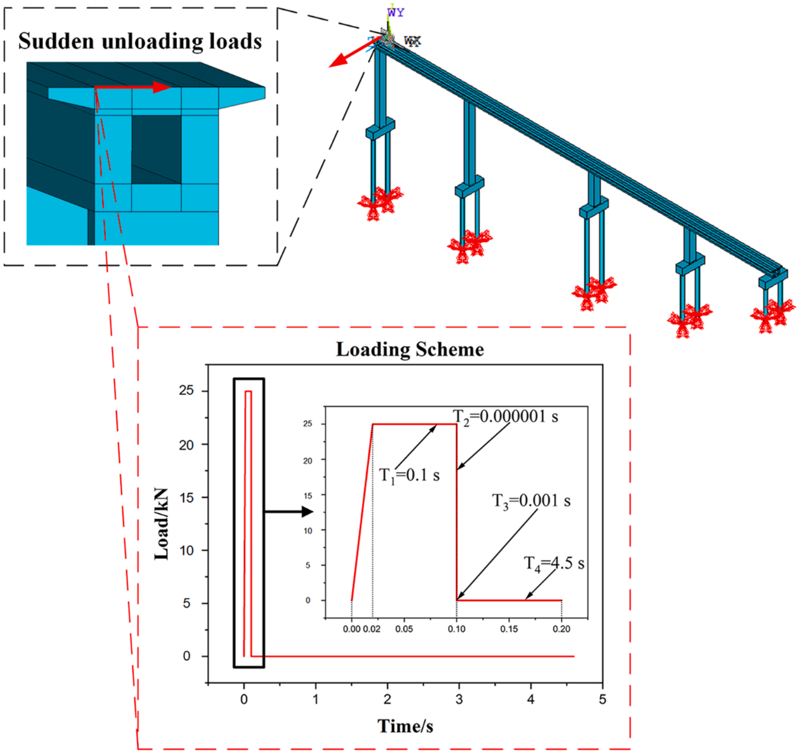

Fig. 6. Four-step loading scheme applied at the left end of the pedestrian bridge.

Table 3
First 10 orders of natural frequencies of the intact FE model.

Order	Natural frequency/Hz	Order	Natural frequency/Hz
1	0.655	6	2.091
2	0.867	7	2.111
3	0.983	8	2.154
4	1.457	9	2.900
5	1.872	10	3.078

were reasonably simplified into 10 different monopile damage conditions and the intact condition. The damage condition settings were shown in Table 1. The intact condition (condition $0^{\#}$) indicated that there was no global structural damage (stiffness degradation) appearing in the pile foundations of the pedestrian bridge. Condition $i^{\#}$ meant that global structural damage only occurs in PF $i^{\#}$, structural stiffness of the corresponding pile foundation was reduced to 25 % of its initial stiffness.

4.3. Numerical simulation

4.3.1. Material properties and modelling process

In this study, a total of 11 FE models of the continuous beam pedestrian bridge was created using ANSYS 19.2, the material parameters used in this simulation are summarized in Table 2.

The SOLID186 element is utilized for constructing the FE model, which is developed using a bottom-up, direct modeling approach. This process involves the following steps: (i) defining single-cell box girder nodes, (ii) creating the single-cell box girder cross-section, (iii) generating a single-cell box girder body, (iv) forming thin-walled pier bodys, (v) constructing bearing platform bodys, and (vi) establishing pile foundation bodys. After these steps, the degrees of freedom (DOFs) of common nodes on the contact surfaces of each body are coupled, and each body is meshed. Each pile foundation, bearing platform, bridge pier, and box girder are divided into 500, 400, 400, and 500 elements, respectively.

The FE model was shown in Fig. 4. Several FE models under different damage conditions were demonstrated in Fig. 5, and the purple elements represent damaged pile foundations.

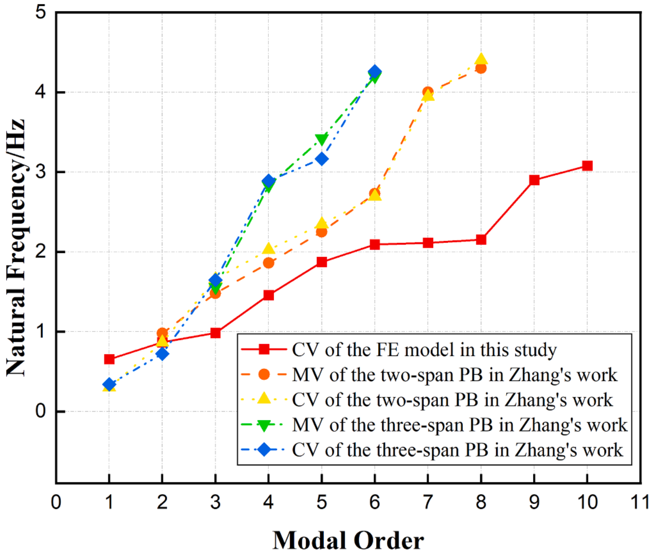

Fig. 7. Comparison of the natural frequencies between the intact FE model in this study and Zhang's work including calculated and measured natural frequencies.

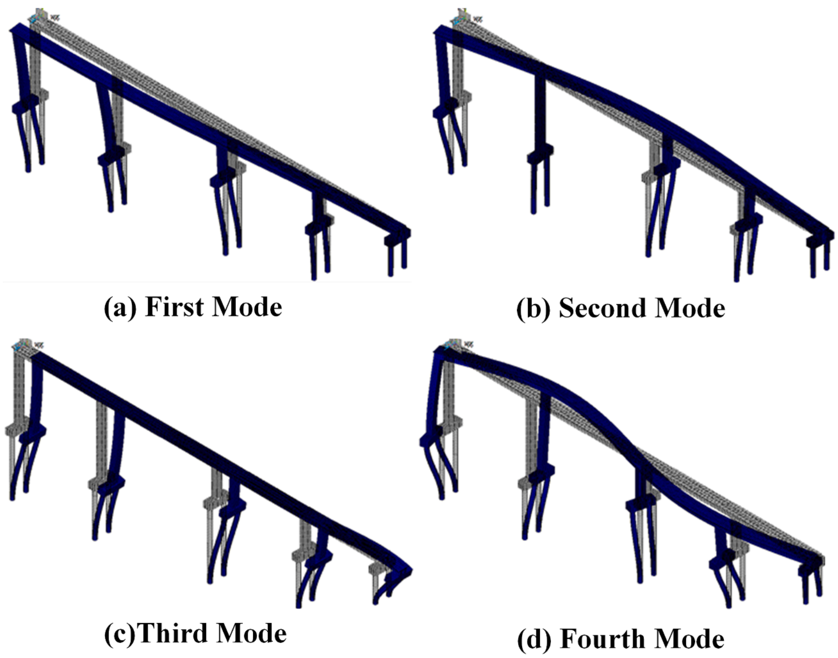

Fig. 8. The first four modes of the FE model of the pedestrian bridge: (a) overall lateral vibration, (b) overall torsional vibration, (c) overall longitudinal vibration, and (d) overall torsional vibration.

4.3.2. Boundary conditions and load scheme

The validity of simplifying the complex interaction between pile foundations and soil by applying fixed constraints to the base of the pile foundations has been confirmed in the literature [46], an approach that is also adopted in this study.

Sudden unloading loads, which are applied at the root of the upper flange of the left end of the box girder, are utilized to excite the pedestrian bridge. Briefly, the loading scheme is divided into 4 steps. Firstly, the loads increase from 0 to 25 KN within 0.1 s and 5 substeps. Secondly, the loads decrease to zero in a ramp-like fashion over 1×10^{-6} s within 50 substeps, which is done to fulfill the convergence criteria of numerical calculations. Next, the third load step divided into 1000 substeps has a duration of 0.001 s while the load is 0. Finally, the fourth step, lasting 4.5 s with 0.01 s for each substep, still has no applied load and represents the free vibration process of the FE model of the pedestrian bridge. The loading position and detailed procedure are further demonstrated in Fig. 6.

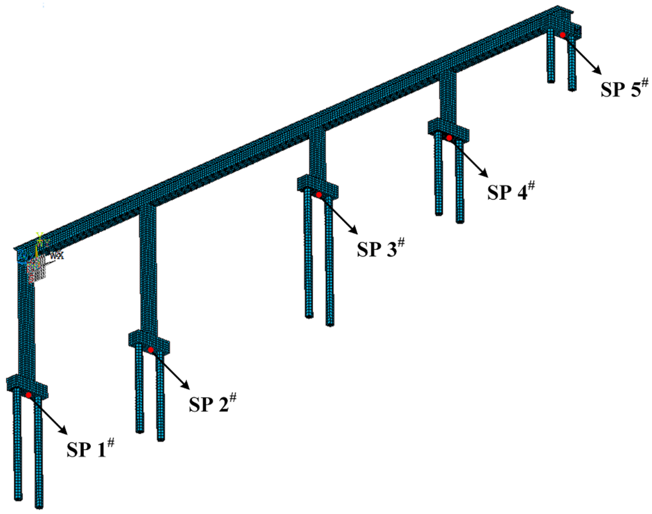

Fig. 9. The five sampling points located at the center of the bottom surface of the bearing platform.

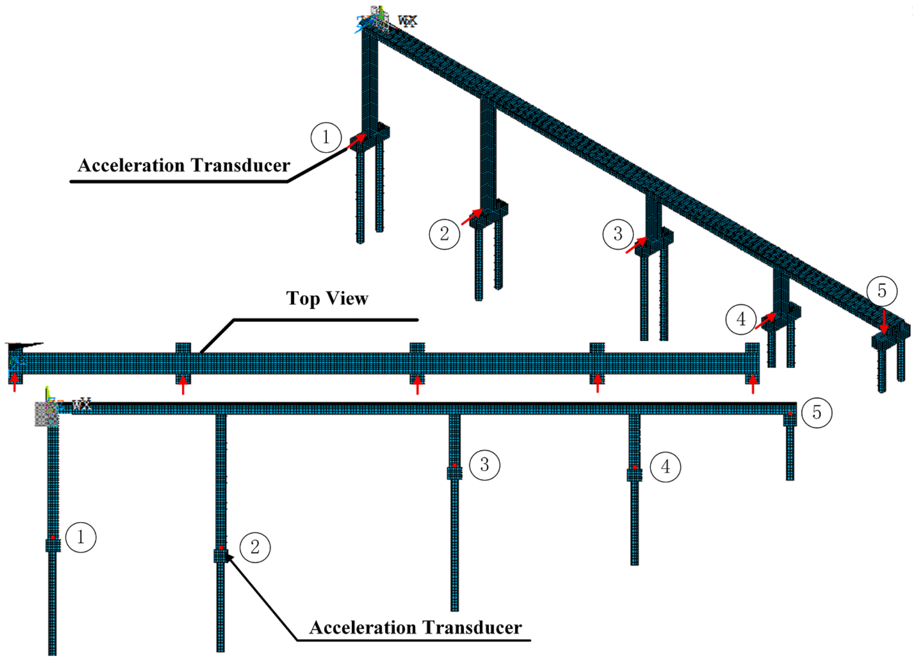

Fig.10. Layout of the arranged accelerometers for on-site ambient vibration measurements.

4.3.3. Dynamic characteristics verification

To verify the rationality of the pedestrian bridge' FE models, modal analysis was performed using the FE model under the intact condition. It needed to be emphasized that the first 10 orders of natural frequencies and modes were utilized as primary indicators.

(1) Natural frequencies

The first 10 orders of natural frequencies calculated via numerical simulation are listed in Table 3. In a previous study, to investigate the evaluation method of vibration comfort of pedestrian bridges, Zhang et al. [60] conducted a substantial amount of field tests and finite element simulations for vibration characteristics of RC continuous beam pedestrian bridges (PB).

The contrasts between calculated values (CV) of the natural frequencies in this study and those derived from the above-mentioned study, measured values (MV) and CV of the natural frequencies from two-span and three-span continuous beam PB, are demonstrated in Fig. 7.

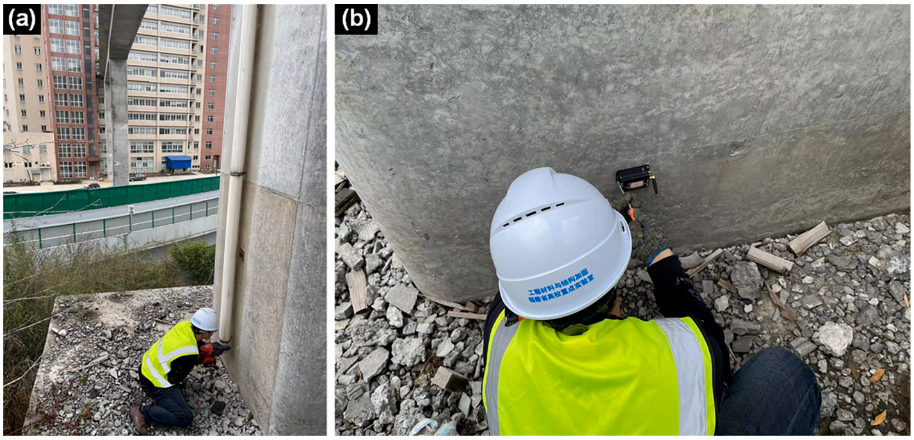

Fig.11. Demonstration of accelerometer installation with (a) the drilling process and (b) the installed accelerometer near the bearing platform.

Through contrast analysis, it can be seen that the first three orders of natural frequencies of the FE model in this work were reasonably close to those MV and CV in Zhang's study. In fact, the first-order natural frequency is also known as the predominant frequency, which is often used as an important parameter for evaluating the rationality and effectiveness of FE models [61–63]. Although a slight increase in the parameter gap between the two studies is observed in the higher orders, the discrepancy in the natural frequencies, caused by differences in the local structure of the pedestrian bridges, remains within an acceptable range.

(2) Modes

The first 4 orders of modes obtained through numerical simulation are shown in Fig. 8 and the remaining modes in the first 10 orders are given in Appendix A.

Regarding the modes, the figures indicate that the first four modes of the pedestrian bridge are respectively manifested as the overall lateral vibration, overall torsional vibration, overall longitudinal vibration, and overall torsional vibration, while the fifth and higher modes are mainly represented as independent local vibration. Indeed, the results are highly consistent with the first several orders of modes of pedestrian bridges reported in Zhang's research [60]. Additionally, the changing trend of the modes of the pedestrian bridge structure from global vibration at lower-order modes to local vibration at higher-order modes, is quite similar to the previous study on the vibration characteristics of high-pile wharf, which is also a kind of structure with similar pile foundations [46].

Therefore, the FE model established in this study for the pedestrian bridge is reliable and valid based on its dynamic properties including natural frequencies and modes.

4.3.4. Sampling scheme

While it is relatively straightforward to obtain dynamic response data from any node of the FE models at any given time, the acceleration response acquisition scheme of the FE model in this paper is designed to accommodate the practicality and accessibility of sensor deployment strategies for field monitoring. Five sampling points, located at the center of the bottom surface of the bearing platform, were selected to gather the acceleration responses. The distribution map of all sampling points of the pedestrian bridge can be viewed in Fig. 9. The transient dynamic calculation process, which spanned 4.6 s, ultimately produced a total of 1479 substeps of acceleration responses, with each substep containing components projected onto the three major axis directions (X, Y, and Z, representing the longitudinal, vertical, and lateral directions of the pedestrian bridge, respectively).

4.4. On-site ambient vibration measurement

The vibration response of the pedestrian bridge can be influenced by pedestrian movement, wind, and nearby traffic, which significantly affects the model's generalization ability in recognizing true cases. Hence, to capture the bridge's response under ambient vibrations, on-site measurements were taken using a configuration of five accelerometers, as depicted in Fig. 10. It is important to note that in the prototype structure, the bearing platforms were buried beneath the foundation. However, due to the minimal response difference between the simulated sampling locations and the junctions of the pier-bearing platform, which are considered a rigid body, it is both effective and more convenient to position the accelerometers at the latter. For this study, 3D accelerometers DiViMeter Env3.1 were utilized, and the installation of the five accelerometers is illustrated in Fig. 11. The acceleration response in the three cardinal directions was recorded at a sampling frequency of 500 Hz over a total duration of four hours with the temperature variates between 19 ℃ and 34 ℃, resulting in a raw data length of 7.2×10^6.

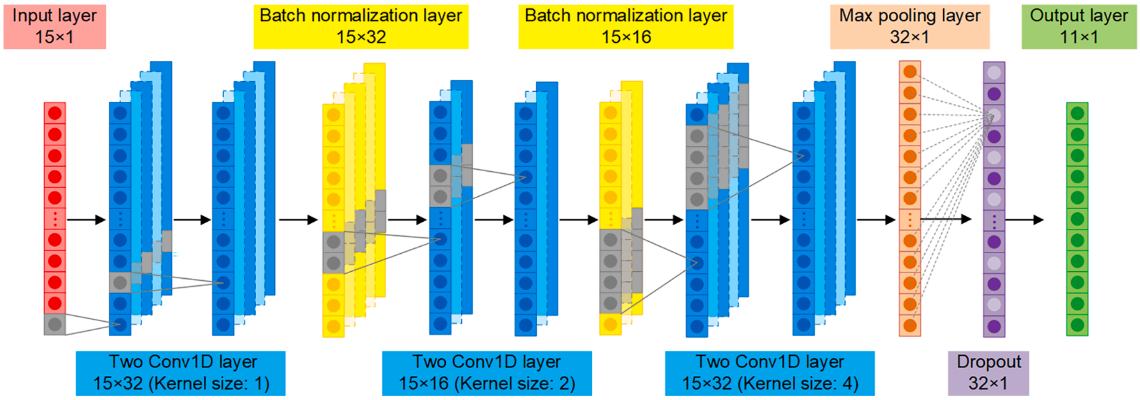

Fig. 12. Overall architecture of the established 1D CNNs trained by 1-timestep samples.

Table 4
Four datasets with different individual sample lengths.

Hyperparameter	Lower limit	Upper limit	Granularity
Convolutional layer neurons	16	128	16
Kernel size	1	8	1
Learning rate	0.005	0.015	0.002
Momentum	0.5	1.0	0.1
Decay rate	0.0001	0.0005	0.0001
Dropout rate	0.1	0.5	0.1

5. The adopted one-dimension convolutional neural network

5.1. A brief overview

Convolutional Neural Networks (CNNs) have emerged as powerful pattern analysis models, largely due to their unique parameter sharing and automatic feature engineering capabilities. These networks have found widespread application in computer vision and time series processing. In particular, 1D CNNs have demonstrated impressive performance in speech recognition, stock price prediction, and text classification in natural language processing, among other areas. Essentially, these networks excel at capturing temporal patterns and local features in sequential data.

It is observed that recent developments in DL have led to the emergence of numerous high-performance network architectures. In unsupervised and semi-supervised learning, large-scale models like generative artificial intelligence have achieved remarkable breakthroughs [64,65]. In supervised learning, traditional neural networks adapted with attention mechanisms have been widely applied in damage recognition [66,67]. These successful applications rely on the accumulation of vast amounts of data and domain knowledge. However, in the context of SHM and/or SDD of complex large-scale structures, obtaining structural responses of known explicit damages is extremely costly or even unavailable in most cases, which results in a limited amount of data for training SDD models. Given these constraints, the choice of 1D CNNs for SDD tasks is based on several factors. Firstly, 1D CNNs have demonstrated promising results in analyzing sequential data, making them well-suited for processing time-series sensor data. Additionally, compared to more complex networks such as recurrent neural networks [68,69] or transformer-based networks [70,71], 1D CNNs offer a simpler architecture and greater computational efficiency, which is advantageous for real-time or resource-constrained applications.

A typical 1D CNNs comprises an input layer, several hidden layers, and an output layer. The hidden layers are usually designed by stacking various layers together, including convolutional layers, pooling layers, batch normalization layers, fully connected layers, and dropout layers, among others.

5.2. Adopted architecture and hyperparameter optimization

In this study, the architecture with local convolutional blocks containing only one convolutional layer was tested, and the results showed that this architecture's model could hardly achieve accuracy beyond random guessing. Stacking multiple convolutional layers can significantly enhance the network's local feature engineering capability but also introduces a rapid increase in training weight parameters, leading to model overfitting and reduced generalization ability. Based on these experiences, several candidate convolutional units and overall network architectures are designed for comparison as demonstrated in Fig. A2 and Fig. A3 in the Appendix. Finally, the overall architecture is determined by the best performance between them, as shown in Fig. 12. The currently employed architecture, which features 10 hidden layers, is an optimized version of the one presented in our previous work [46], where we describe the function of each type of layer in detail.

Table 5
Four datasets with different individual sample lengths.

Group	Forms of individual sample	Number of samples	Size of each sample
1	$(\mathrm{ACC}^{\mathrm{n}}_{\mathrm{spX}}, \mathrm{ACC}^{\mathrm{n}}_{\mathrm{spY}}, \mathrm{ACC}^{\mathrm{n}}_{\mathrm{spZ}}, \cdots, i), n = 1$	4950	15
2	$(\mathrm{ACC}^{\mathrm{n}}_{\mathrm{spX}}, \mathrm{ACC}^{\mathrm{n}}_{\mathrm{spY}}, \mathrm{ACC}^{\mathrm{n}}_{\mathrm{spZ}}, \cdots, i), n = 1, 2$	2475	30
3	$(\mathrm{ACC}^{\mathrm{n}}_{\mathrm{spX}}, \mathrm{ACC}^{\mathrm{n}}_{\mathrm{spY}}, \mathrm{ACC}^{\mathrm{n}}_{\mathrm{spZ}}, \cdots, i), n = 1, 2, 3$	1650	45
4	$(\mathrm{ACC}^{\mathrm{n}}_{\mathrm{spX}}, \mathrm{ACC}^{\mathrm{n}}_{\mathrm{spY}}, \mathrm{ACC}^{\mathrm{n}}_{\mathrm{spZ}}, \cdots, i), n = 1, 2, 3, 4$	1232	60

Remark: The left subscript **sp** represents the sampling points from 1 to 5, the right subscript **(X, Y, Z)** represent the direction of the acceleration components, and the superscript **n** represents the number of the substeps in one sample.

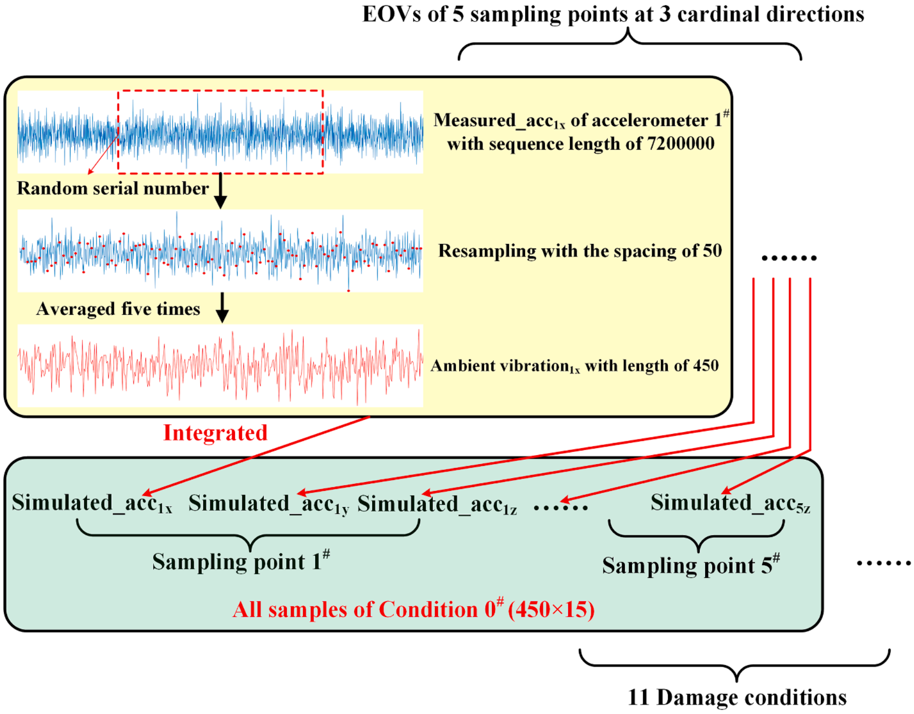

Fig. 13. Detailed procedures of on-site measurement processing and the data fusion process: the yellow block shows the EOVs generated from the raw measurement and the green block contains simulated responses at five sampling points under the intact condition, the red arrow means the fusion operation. The fusion process of remaining damaged conditions has been omitted due to space constraints. (For interpretation of the references to colour in this figure legend, the reader is referred to the web version of this article.)

In addition, the impact of the structure of training samples on the performance of the models is also investigated. To this end, we construct four datasets with different individual sample lengths, namely, 1-timestep, 2-timestep, 3-timestep, and 4-timestep. Each timestep encapsulates acceleration components at five sampling points in three directions. It's crucial to note that while the four models share the same overall architecture, the parameters shown in Fig. 12 exclusively illustrate the model trained by 1-timestep samples.

Besides, hyperparameters are optimized based on the model's performance on the validation set. The main hyperparameters include the number of neurons in convolutional layers, the size of convolutional kernels, learning rate, learning rate momentum, learning rate decay, and the dropout rate of dropout layers. Specifically, the number of neurons in the convolutional layers is set to decrease layer by layer from the input layer, then gradually increase after passing the middle layer, while the size of the convolutional kernels is set to increase layer by layer. All hyperparameters are optimized using an orthogonal search strategy. The range of hyperparameter optimization in this study is shown in the Table 4:

The training and validation processes are further elaborated in the following Section 6.3.

6. CNNs-based damage detection method

In this study, both simulated and measured acceleration responses are utilized to develop the proposed enhanced 1D CNNs-based damage localization procedure.

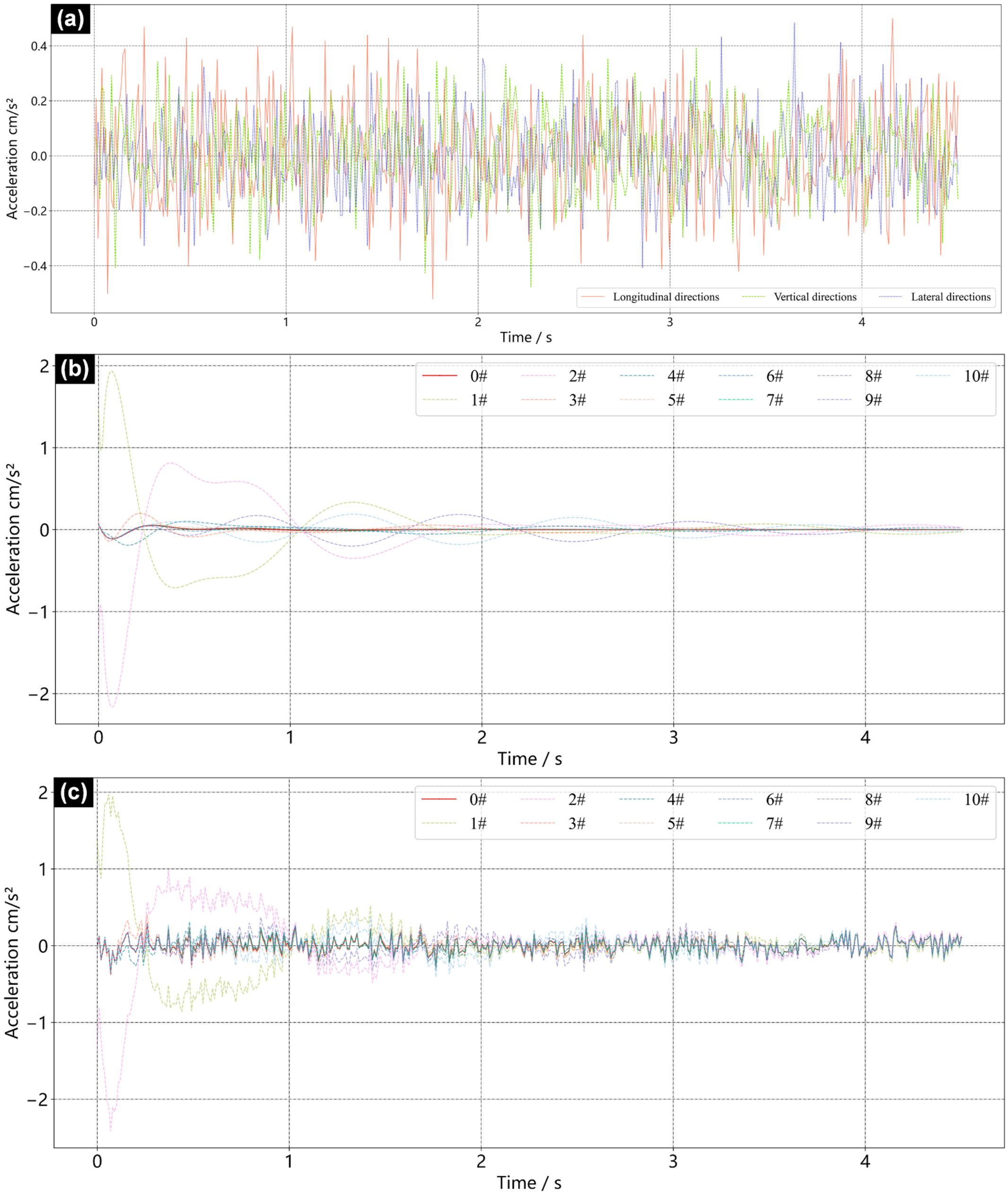

Fig. 14. An example of the simulated response-EOVs fusion process: (a) EOVs of accelerometer $1^{\#}$ at three directions and (b) simulated responses of sampling point $1^{\#}$ in the longitudinal direction and (c) fusion responses in the longitudinal direction.

6.1. Different datasets construction

For the simulated data of each damage condition, the last 450 substeps of the total 1479 substeps of the time series have a more significant change which corresponds to the free vibration stage after the sudden unloading. Next, these 450 substeps data within the last 4.5 s are used to construct four different datasets demonstrated in Table 5 as Section 5 mentioned, for example, the individual sample of group (1) consists of three acceleration components of all five sampling points in 1-timestep which result in a total of 4950 samples of the first dataset. The arrangement of each item in the individual sample has been illustrated in detail in Table 5.

6.2. Details of the data fusion process

The details of the data fusion process will be elaborately described in this section. Indeed, the acceleration response caused by ambient vibration is usually two orders of magnitude smaller than those resulting from loading. However, ambient vibration is one of

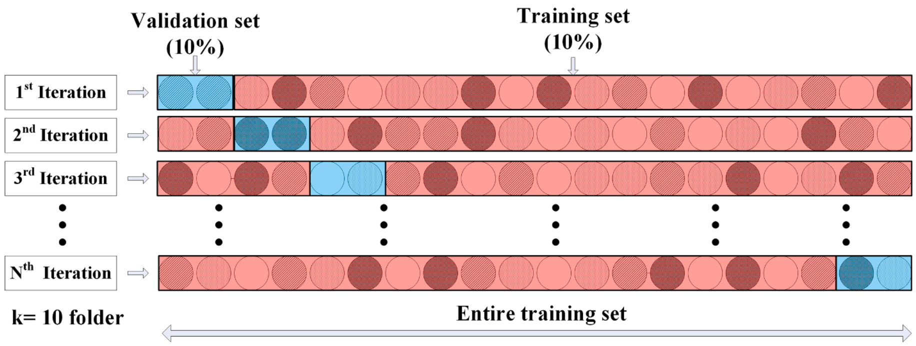

Fig. 15. Schematic of the K-Fold cross-validation.

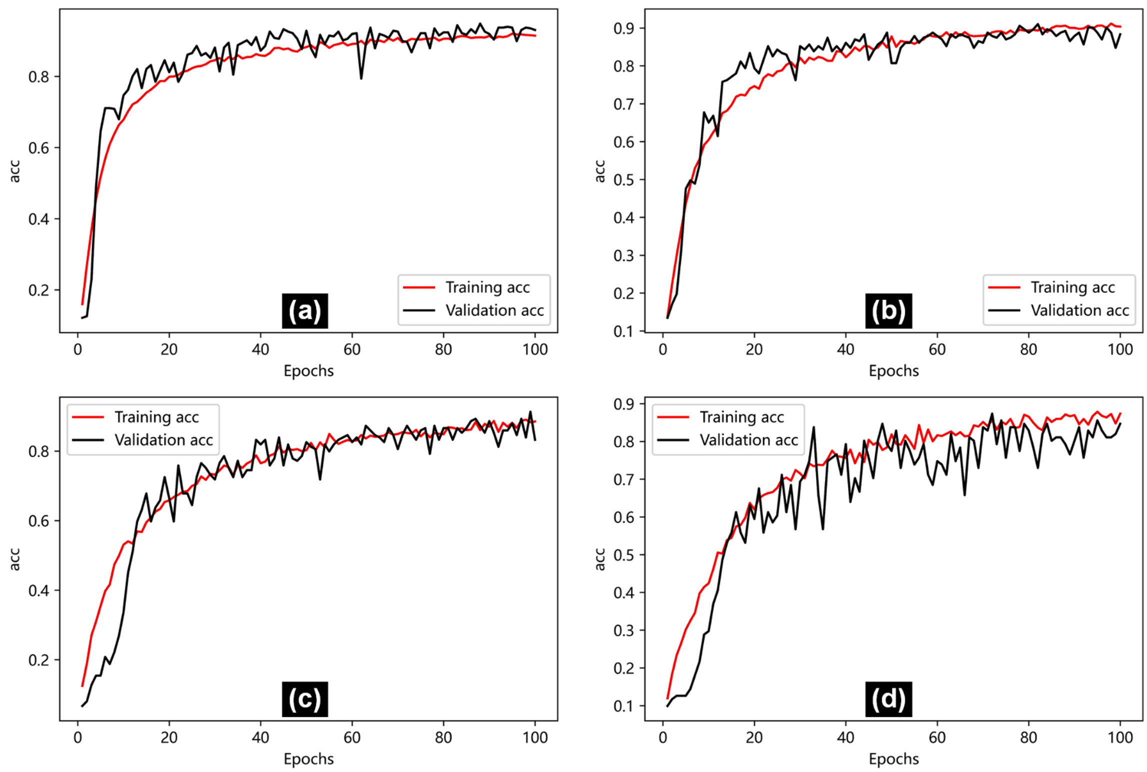

Fig. 16. Training and validation accuracy curves of four baseline 1D CNN models in 100 epochs trained by simulated training sets with varying sample lengths: (a) 1-timestep samples, (b) 2-timestep samples, (c) 3-timestep samples, (d) 4-timestep samples.

the most influential factors for the robustness and generalization of most DL models, especially those trained solely on simulated data. This is crucial when these models are applied to real-world scenarios where EOVs must be considered [4,72,73]. To eliminate drawbacks in previous work [46], the on-site measured acceleration response of intact prototype structure with ambient vibration is processed as EOVs superimposed into the simulated acceleration, the processing procedures are summarized in Fig. 13. It should be noted that the different levels of EOVs will undoubtedly affect the performance of the SDD model, however, due to budget constraints, this study only utilizes short-term on-site measurements to account for the EOVs induced by ambient vibration.

The following describes the procedure for the simulated acceleration of SP SP $1^{\#}$ under condition $0^{\#}$, although the remaining operations are similar. Initially, the raw measured acceleration in the X direction from accelerometer $1^{\#}$, subsequently denoted as 'measured_acc$_{1x}$', is truncated at a random starting point to a sequence length of 22,500 (50 $\times$ 450). Next, 'ambient_vibration$_{1x}$' is derived by resampling the truncated fragment with a spacing of 50 and averaging it over five repetitions. Finally, this 'ambient_vibration$_{1x}$' is superimposed onto the 'simulated_acc$_{1x}$', and the process is repeated for the three directions of all five sampling points. It is crucial to emphasize that the 15 EOVs sequences differ within a single condition but are reused across different conditions.

For clarity, a specific example is provided in Fig. 14 to illustrate the fusion process of the simulated response with EOVs. Due to space constraints, the remaining figures related to this operation are not included in this paper but are available upon request.

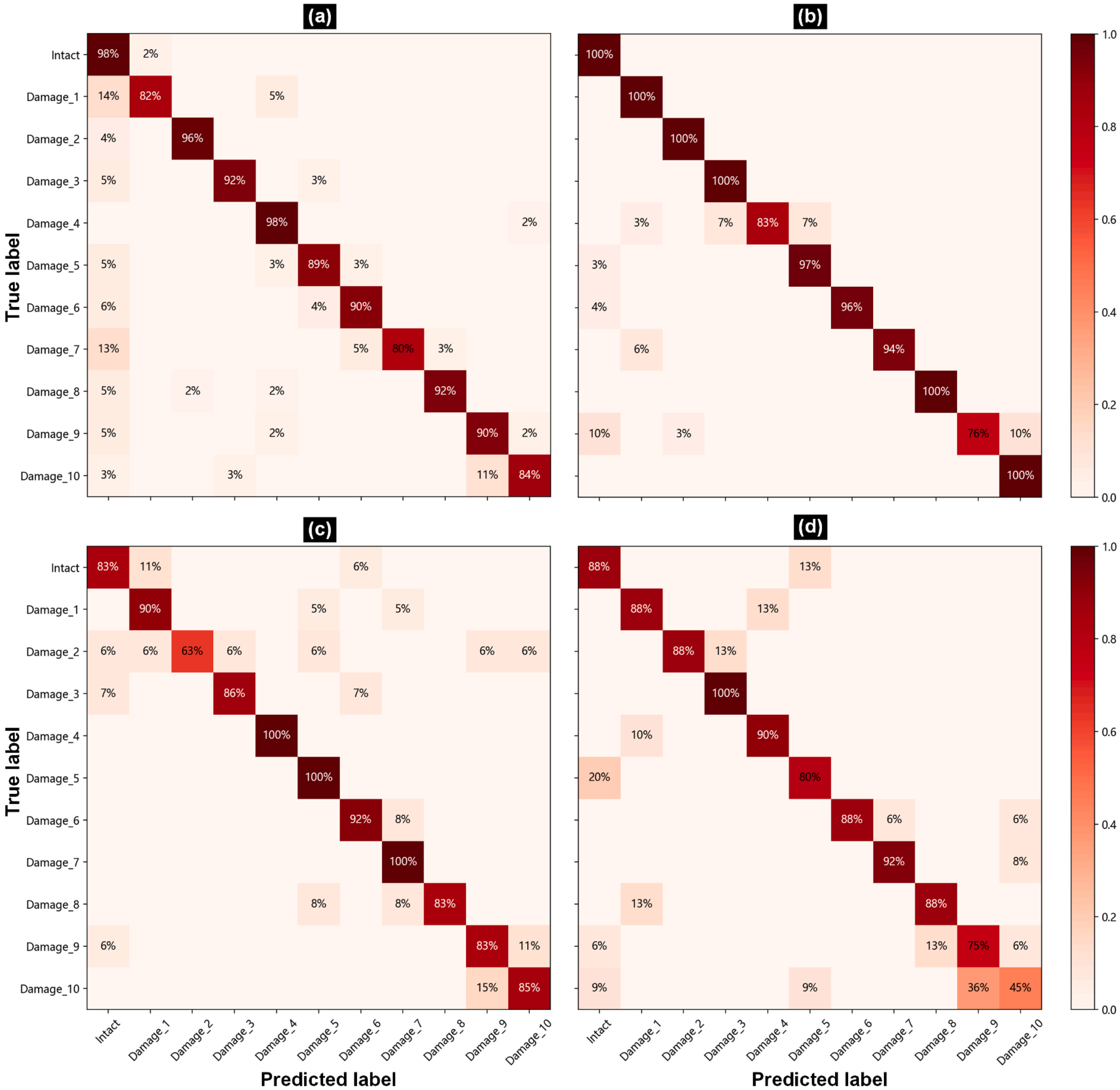

Fig. 17. Confusion matrixes of four baseline 1D CNN models tested on simulated testing sets with varying sample lengths: (a) 1-timestep samples, (b) 2-timestep samples, (c) 3-timestep samples, (d) 4-timestep samples.

6.3. The training and validation processes

As the schematic diagram shows in Section 3, the baseline model is trained by pure simulated data while the reference model is trained by the fusion of simulated acceleration and ambient vibration with EOVs. Therefore, the following demonstration will be divided into two parts:

(1) the baseline model based on pure simulated data

The total samples of all conditions are randomly split into 90 % and 10 %, as the training set and the testing set, respectively. The entire training set is continually randomly divided into 90 % and 10 % as the training set and validation set during each iteration. In this study, the initial value of the learning rate is set at 0.0001, then it is updated simultaneously within the training process. The batch of the training sample is set as 128 and the training epochs are set as 100. The K-Fold cross-validation [74] is utilized in this process with the brief illustration shown in Fig. 15. Moreover, the aforementioned processes are the same for the four datasets with different individual sample lengths.

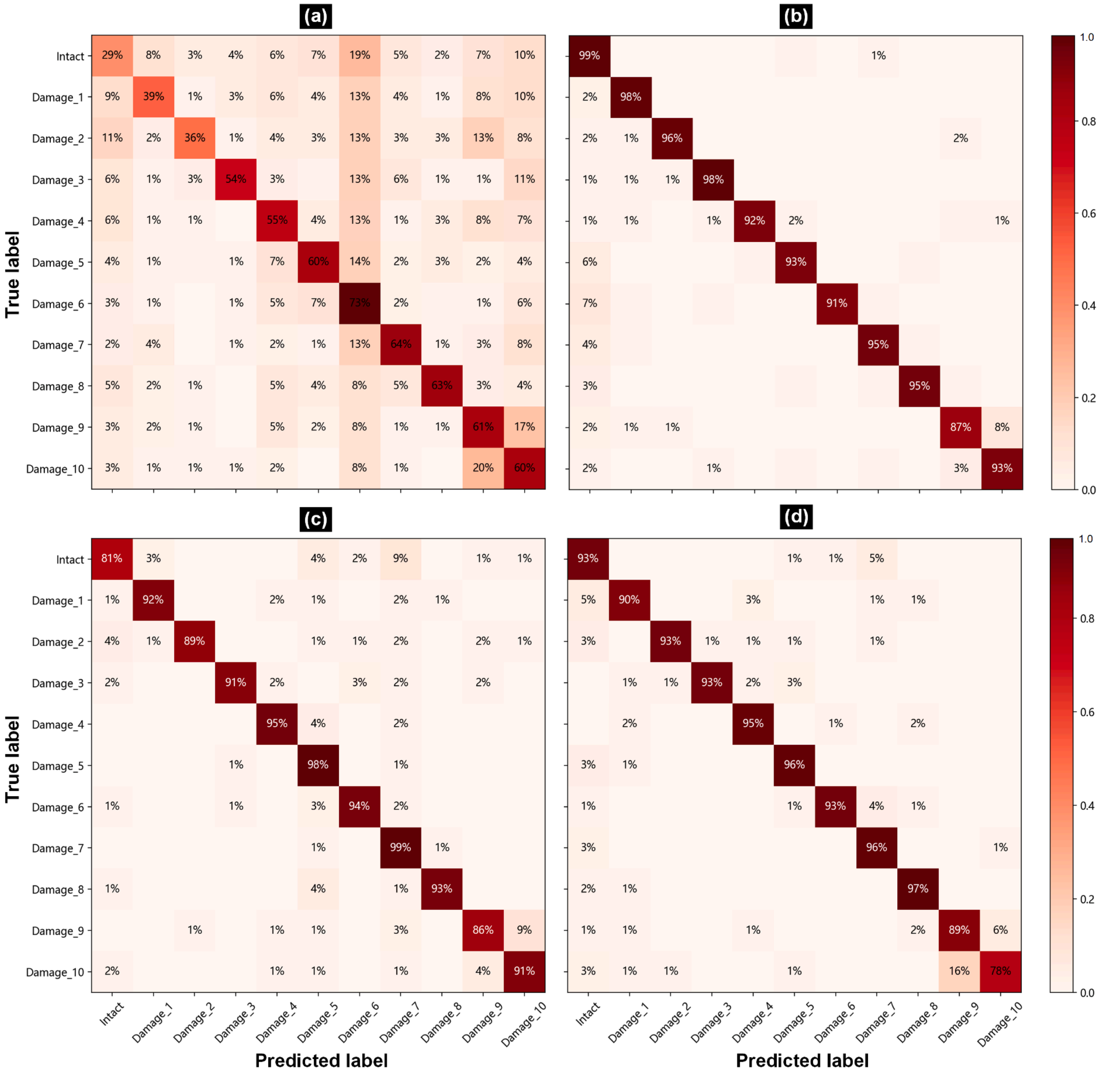

Fig. 18. Confusion matrixes of four baseline 1D CNN models tested on fusion testing sets with varying sample lengths: (a) 1-timestep samples, (b) 2-timestep samples, (c) 3-timestep samples, (d) 4-timestep samples.

(2) the reference model based on part-fusion data

Before proceeding with a detailed introduction, it is crucial to clarify that measuring the ambient vibration of intact structures is relatively straightforward in engineering practice. For example, newly constructed structures are often regarded as intact objects. Conversely, obtaining ambient vibration from structures with deterministic damage is considerably more challenging. Therefore, to enhance the practicality of the proposed damage detection method, EOVs are only added to the samples of condition $0^{\#}$ (intact condition) during the training and validation process. However, all categories of samples with EOVs are used in the testing process to further validate the model's performance in identifying damage, considering the interference factor of EOVs.

It is noted that the introduction of measured EOVs during the training phase essentially serves as a physical guide to the training process for the SDD model, enhancing the model's generalization ability during actual application.

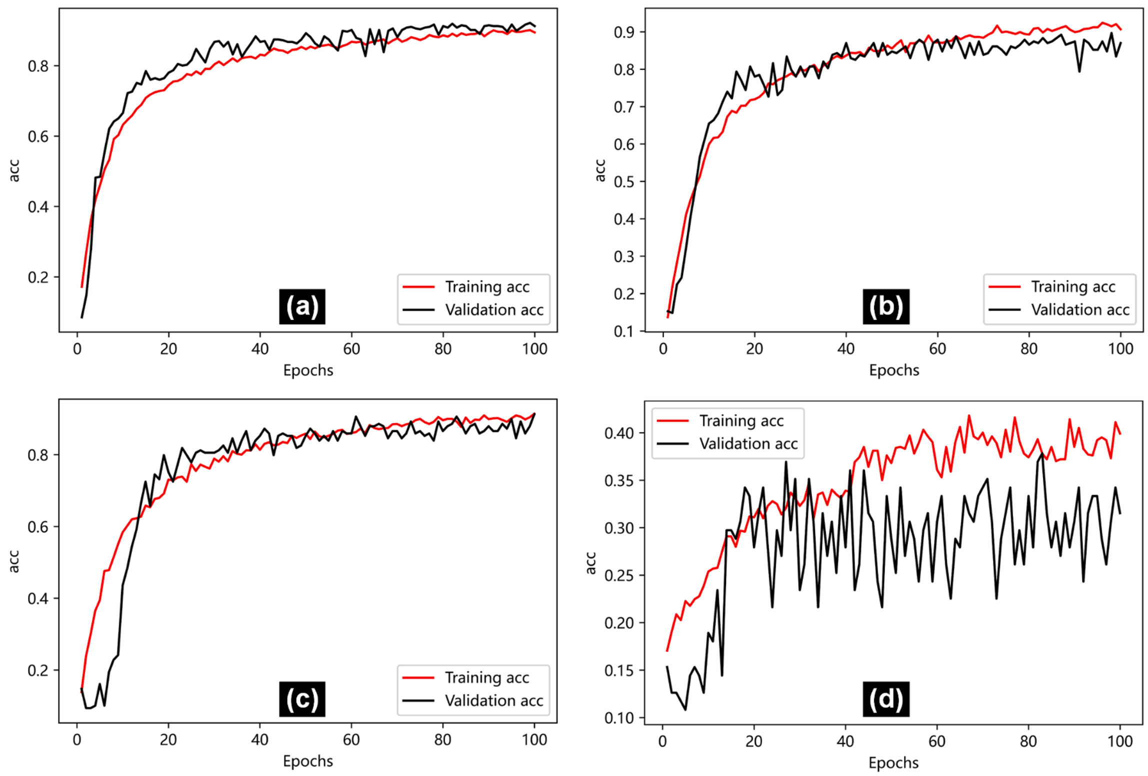

Fig. 19. Training and validation accuracy curves of four reference 1D CNN models in 100 epochs trained by part-fusion training sets with varying sample lengths: (a) 1-timestep samples, (b) 2-timestep samples, (c) 3-timestep samples, (d) 4-timestep samples.

7. Results and discussions

7.1. Performance of baseline model on simulated data

The training and validation history curves of the four baseline 1D CNN models based on samples with varying lengths and the corresponding confusion matrixes on the testing sets are shown in Fig. 16 **and** Fig. 17, respectively. It can be observed in Fig. 16 that (a) the first two baseline models perform better on the validation accuracy than the other two models within 100 epochs, in turn, 92.1 %, 91.3 %, 85.9 % and 86.2 %; (b) the first two models achieve relatively high accuracy within 10 epochs which faster than the other two models and the over-fitting occurs during training of the last baseline model due to fewer samples shown in Table 4. On the other hand, the confusion matrixes indicate that the second baseline model shows excellent classification accuracy (95.09 %) on the testing set than the others (90.10 %, 87.73 %, 83.81 %). However, there are still some samples of damage conditions predicted as the intact condition, this phenomenon called a false negative is a risk for SHM/SDD in engineering practice.

7.2. Performance of baseline model on fusion data

To further verify the robustness and generalization of the four baseline models, all fusion data introduced in Fig. 13 is used as the testing set to obtain the following fusion matrixes listed in Fig. 18. It can be found that the overall testing accuracies of four baseline model on fusion data are 54.10 %, 94.27 %, 91.73 % and 92.09 %, respectively. Except for the first baseline model which performs poorly, the other three baseline models all behave well which indicates they are highly robust in identifying damage with EOVs. However, the issue of false negative predictions persists.

7.3. Performance of reference model on part-fusion data

To optimally utilize the fusion data, four new reference 1D CNN models are established with the same architecture. These models are trained on the partial fusion dataset, which comprises fusion data from the intact condition and simulated data from 10 damage conditions. The rationale behind this approach is explained in Section 6.3. Similarly, the history curves and corresponding confusion matrices for the partial fusion dataset are shown in Fig. 19 and Fig. 20, respectively. The training processes closely resemble those of the baseline models, except for the last reference model, which exhibits severe overfitting leading to poor training and validation accuracy.

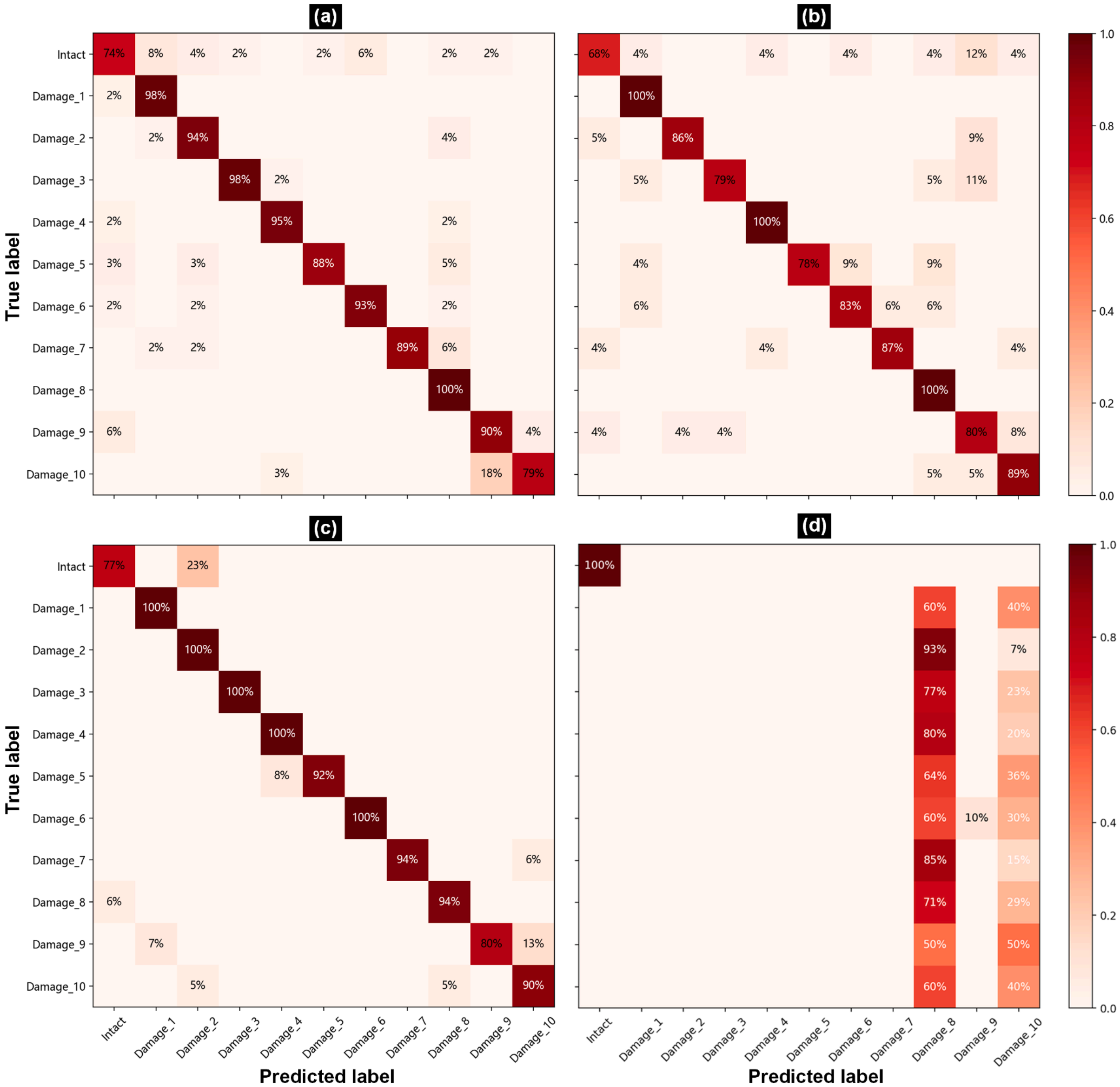

Fig. 20. Confusion matrixes of four reference 1D CNN models tested on part-fusion testing sets with varying sample lengths: (a) 1-timestep samples, (b) 2-timestep samples, (c) 3-timestep samples, (d) 4-timestep samples.

According to the confusion matrices, the overall testing accuracies of the four reference models on the partial fusion data are 90.73 %, 88.18 %, 93.36 %, and 19.18 %, respectively. The performances of the first two reference models closely match those of the first two baseline models. The third reference model performs significantly better in overall classification accuracy, but is prone to predicting intact samples as damaged ones, resulting in a false positive rate of 23 %.

Finally, it is noteworthy that the false negative/positive rates of the last reference model are both 0. This suggests that it could be a potent model for differentiating between intact and damaged conditions. Its notably low overall performance is attributed to overfitting, caused by a relatively small number of training samples.

7.4. Performance of reference model on full-fusion data

As the testing carried out in Section 7.2, the above four reference models are also tested using the full-fusion dataset, the confusion matrixes are shown in Fig. 21. It is clear that the overall performance is unsatisfactory which could be explained by the fact that, only the samples of intact condition fused with EOVs while the other samples are all pure simulated response, which results in the increasing of the false negative results and more broadly dispersed wrong predictions.

However, a silver lining can be found in Fig. 21(d). The false negative/positive rates of the last reference model tested on the full-

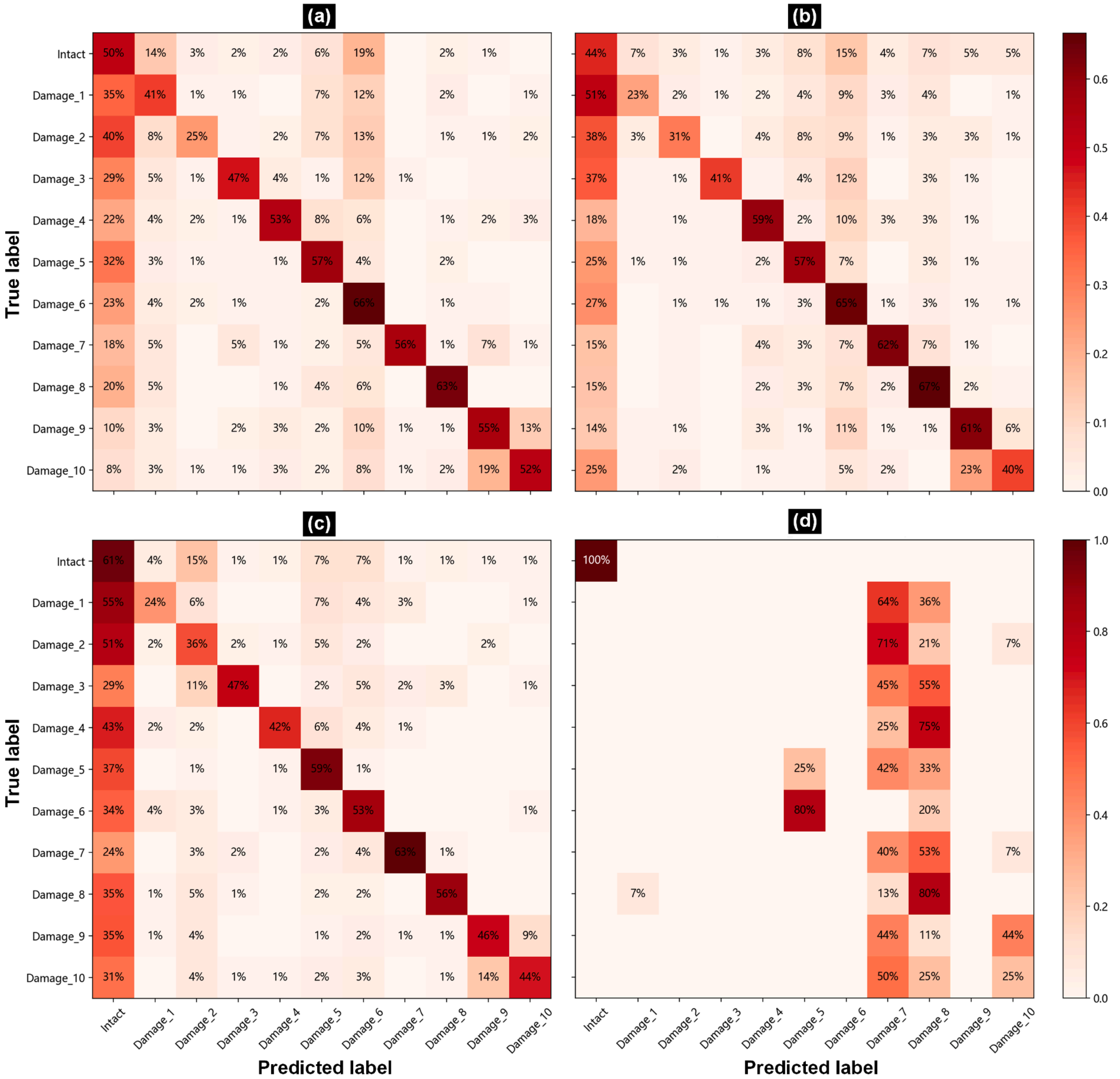

Fig. 21. Confusion matrixes of four reference 1D CNN models tested on full-fusion testing sets with varying sample lengths: (a) 1-timestep samples, (b) 2-timestep samples, (c) 3-timestep samples, (d) 4-timestep samples.

fusion dataset are still 0, which confirms its competence in playing the role of a binary (intact/damage) indicator for the damage identification task. Taking this into account, a novel two-stage robust strategy that combines simulated responses and on-site measurements for damage detection in the RC pedestrian bridge is proposed in the subsequent section.

7.5. Proposed novel two-stage robust strategy for damage localization

As the schematic diagram indicates in Fig. 22, the entire process can be bifurcated into two stages. The initial stage detects the presence of damage, while the subsequent stage identifies the damage location by classifying the damage conditions.

Firstly, independent fusion samples, each of a length of four timesteps, are utilized as input for the second reference 1D CNN model. This model essentially functions as a binary indicator, segregating the samples into two categories: intact and damaged. As inferred from the previous results, the presence of damage can be accurately determined due to the zero false negative/positive rate. This not only mitigates the potential risks of erroneously assessing damaged structures as intact but also reduces the maintenance costs associated with repairing structures wrongly evaluated as damaged. Subsequently, each damaged sample is divided into two equally long samples, which are then evaluated by the updated baseline model sequentially. It is important to note that the updated baseline model, which is a retrained version of the previous second baseline model, is based on a partially simulated dataset that only contains

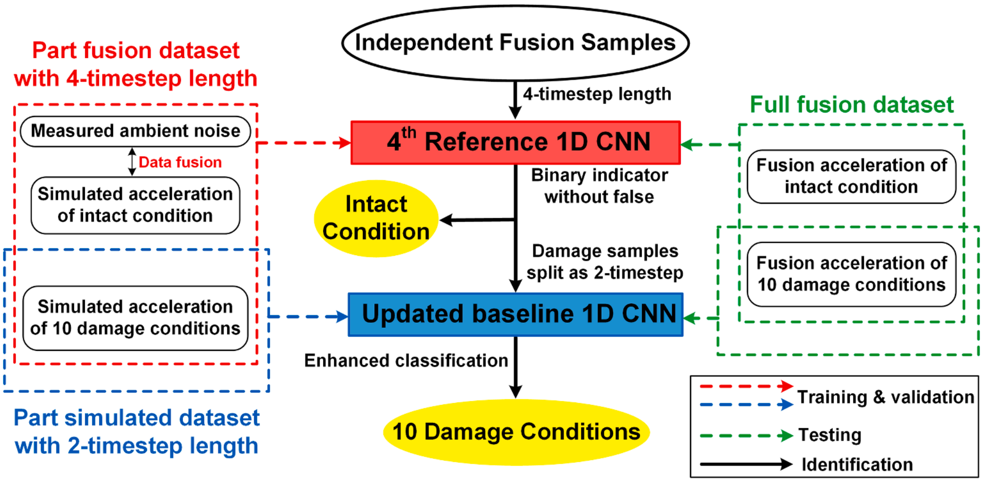

Fig. 22. Schematic diagram of the proposed novel two-stage model ensemble damage localization procedure.

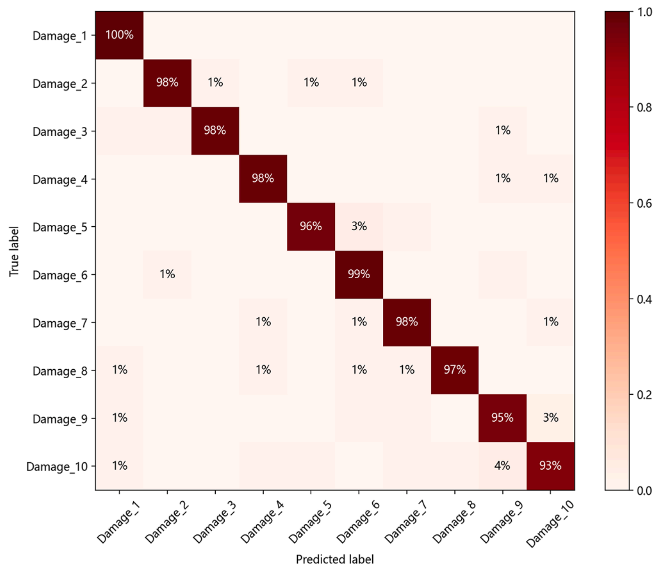

Fig. 23. Confusion matrixes of updated 1D CNN for enhanced damage classification tested on full-fusion testing set.

samples of 10 damage conditions. The confusion matrix of the updated 1D CNN model, shown in Fig. 23, demonstrates an exceptional overall classification accuracy of 97.2 %, marking a significant improvement over the results displayed in Fig. 18**b**.

Notably, most current research related to ML/DL-based VSDD for large-scale infrastructures focuses on validating the effectiveness of the algorithms [39,41–45], while insufficient consideration has been given to the impact of EOVs from the real environment on such approaches. The above results of this study indicate that the presence of EOVs significantly affects the performance of models trained solely on simulated data, particularly in large-scale infrastructure structures. Furthermore, while a previous study [23] has taken into account the impact of EOVs on damage detection performance, a crucial issue has been overlooked: this influence is not only reflected in a decrease in identification accuracy, but also manifests in a significant increase in the false negative rate. Such an increase in the false negative rate is unacceptable in practical engineering scenarios as it may lead to outcomes biased towards risk.

In conclusion, the proposed novel two-stage robust strategy for damage localization optimizes the use of on-site measurements, effectively eliminates false negative/positive predictions, and significantly enhances the accuracy of damage condition identification. Furthermore, the updated baseline 1D CNN model demonstrates substantial robustness and generalization ability when transitioning from a pure simulated dataset to a fusion dataset with EOVs. It should be noted that this study only utilizes short-term on-site measurements to account for the EOVs induced by ambient vibration due to budget constraints. The influence of different levels of EOVs on the performance of the SDD model will be further investigated based on long-term on-site monitoring data in near future.

8. Conclusions

This paper introduces a hybrid damage localization framework based on 1D CNN for a reinforced concrete (RC) pedestrian bridge. It combines simulated acceleration responses from validated finite element (FE) models under 11 orthogonal damage scenarios and short-term ambient vibration measurements containing EOVs of an intact structural prototype. Following an intricate data fusion process, four baseline/reference 1D CNNs models are trained and validated on both purely simulated and partially fused datasets comprising samples of varying lengths. The framework culminates in a two-stage multi-model ensemble strategy for damage localization, with emphasis on safety-oriented, enhanced identification capabilities, and high robustness. The key conclusions are as follows:

(1) This study presents a 1D CNNs-based approach for the damage localization of a typical large-scale RC pedestrian bridge. The results validated the feasibility of the 1D CNNs to automatically learn damage-sensitive features directly from the raw acceleration response data with short-term measured EOVs. Consequently, the proposed framework holds considerable promise for the real-time SHM of civil infrastructures.
(2) The short-term ambient vibration measurements from an intact structural prototype could effectively enhance the performance of the 1D CNNs-based damage localization models trained on simulated responses.
(3) Two-timestep and four-timestep, serving as the individual sample length of the baseline/reference model, exhibit the best performance in damage localization and identification, respectively. Notably, the optimal length of individual samples in different cases needs to be further explored.
(4) The baseline/reference 1D CNNs models demonstrate superior performance on their specific test sets but are less effective on the comprehensive fusion dataset, highlighting the limitations of using a single 1D CNN model for damage detection in real engineering environments with short-term measured EOVs.
(5) The proposed multi-1D CNNs ensemble strategy for damage localization represents a novel and judicious approach, enhancing the use of on-site vibration measurements in two significant ways:
    (i) Safety-oriented Identification: It effectively eliminates false negative/positive predictions, reducing the risk of incorrect evaluations and saving costs on unnecessary maintenance of intact structures;
    (ii) Enhanced Damage Localization: It significantly improves the accuracy of localizing damage conditions, achieving up to 97.2 % accuracy, and the updated baseline 1D CNNs model demonstrates high robustness and adaptability when transitioning from a purely simulated dataset to a fusion dataset that includes short-term measured EOVs, effectively accounting for real engineering environments.

CRediT authorship contribution statement

Yujue Zhou: Writing – review & editing, Writing – original draft, Visualization, Validation, Supervision, Software, Resources, Methodology, Investigation, Funding acquisition, Formal analysis, Data curation, Conceptualization. **Yongcheng Liu:** Writing – original draft, Visualization, Validation, Software, Methodology, Investigation, Formal analysis, Conceptualization. **Yuezong Lian:** Formal analysis, Data curation. **Tanbo Pan:** Formal analysis, Data curation. **Yonglai Zheng:** Investigation, Formal analysis. **Yubao Zhou:** Investigation, Formal analysis.

Declaration of competing interest

The authors declare that they have no known competing financial interests or personal relationships that could have appeared to influence the work reported in this paper.

Data availability

Data will be made available on request.

Acknowledgements

This research received support from the Natural Science Foundation of Fujian Province (Grant No. 2022J011185) and the Fujian Provincial Department of Education (JAT210421). Additionally, Yongcheng Liu and Yubao Zhou extend their gratitude for the financial assistance provided by the China Scholarship Council (CSC).

Appendix A

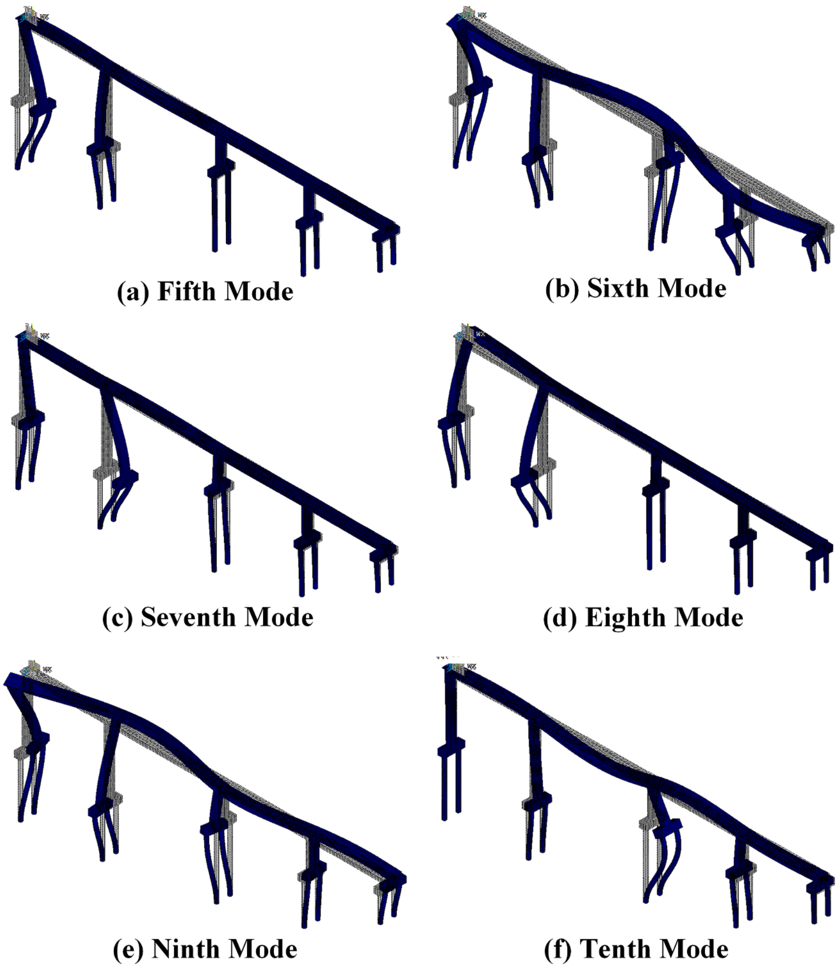

Fig. A1. The fifth to tenth order modes of pedestrian bridge.

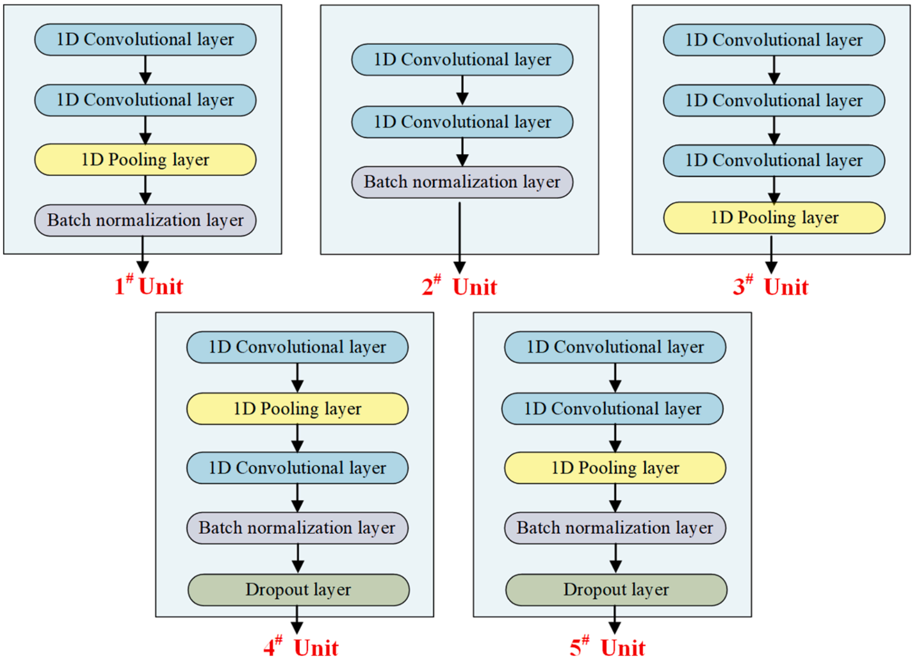

Fig. A2. The five candidate convolutional units.

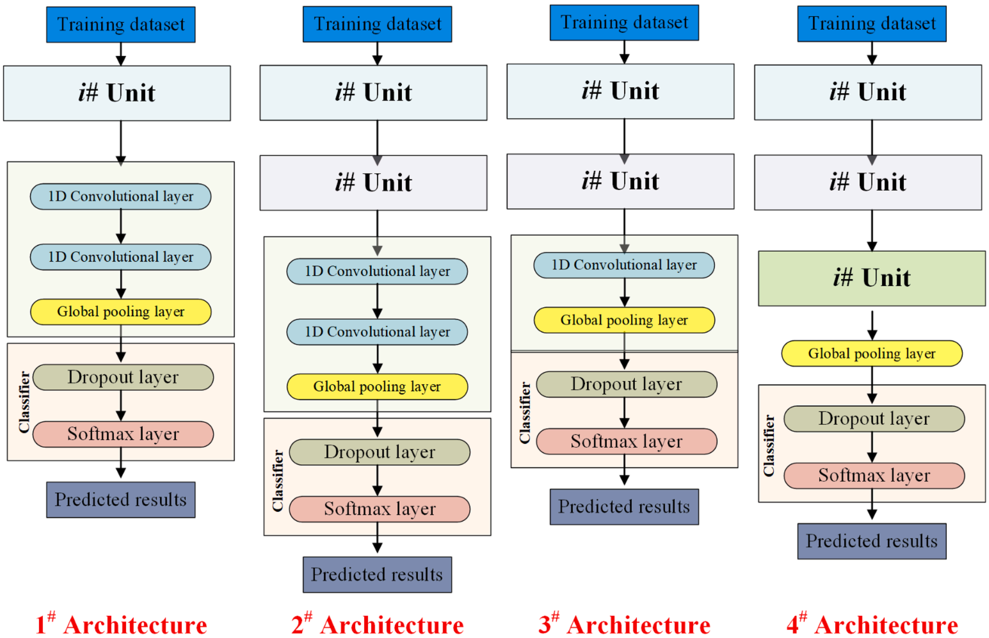

Fig. A3. The four candidate overall architectures of the 1D CNNs.

References

[1] D. Peduto, F. Elia, R. Montuori, Probabilistic analysis of settlement-induced damage to bridges in the city of Amsterdam (The Netherlands), Transp. Geotech. 14 (2018) 169–182, https://doi.org/10.1016/j.trgeo.2018.01.002.

[2] C. Cismaşiu, F.P.A. Santos, R.A.D.S. Perdigão, V.M.S. Bernardo, P.X. Candeias, A.R. Carvalho, L.M.C. Guerreiro, Seismic vulnerability assessment of a RC pedestrian crossing, J. Earthq. Eng. 24 (2020) 727–744, https://doi.org/10.1080/13632469.2018.1453399.

[3] W. Shao, X. He, D. Shi, Durability life prediction of RC piles subjected to localized corrosion in chloride environments, Eng. Fail. Anal. 136 (2022) 106184, https://doi.org/10.1016/j.engfailanal.2022.106184.
[4] E. Figueiredo, J. Brownjohn, Three decades of statistical pattern recognition paradigm for SHM of bridges, Struct. Health Monit. 21 (2022) 3018–3054, https://doi.org/10.1177/14759217221075241.
[5] S.W. Doebling, C.R. Farrar, M.B. Prime, A summary review of vibration-based damage identification methods, Shock Vibr. Digest 30 (1998) 91–105.
[6] J.M.W. Brownjohn, A. De Stefano, Y.-L. Xu, H. Wenzel, A.E. Aktan, Vibration-based monitoring of civil infrastructure: challenges and successes, J. Civil Struct. Health Monit. 1 (2011) 79–95, https://doi.org/10.1007/s13349-011-0009-5.
[7] D. Milanoski, G. Galanopoulos, D. Zarouchas, T. Loutas, Multi-level damage diagnosis on stiffened composite panels based on a damage-uninformative digital twin, Struct. Health Monit. 22 (2023) 1437–1459, https://doi.org/10.1177/14759217221108676.
[8] C.R. Farrar, K. Worden, An introduction to structural health monitoring, Philos. Trans. R. Soc. A Math. Phys. Eng. Sci. 365 (2006) 303–315, https://doi.org/10.1098/rsta.2006.1928.
[9] Y. An, E. Chatzi, S.-H. Sim, S. Laflamme, B. Blachowski, J. Ou, Recent progress and future trends on damage identification methods for bridge structures, Struct. Control Health Monit. 26 (2019) e2416.
[10] O. Avci, O. Abdeljaber, S. Kiranyaz, M. Hussein, M. Gabbouj, D.J. Inman, A review of vibration-based damage detection in civil structures: From traditional methods to Machine Learning and Deep Learning applications, Mech. Syst. Sig. Process. 147 (2021) 107077, https://doi.org/10.1016/j.ymssp.2020.107077.
[11] R. Hou, Y. Xia, Review on the new development of vibration-based damage identification for civil engineering structures: 2010–2019, J. Sound Vib. 491 (2021) 115741, https://doi.org/10.1016/j.jsv.2020.115741.
[12] Development in vibration-based structural damage detection technique, Mechanical Systems and Signal Processing 21 (2007) 2198–2211. https://doi.org/10.1016/j.ymssp.2006.10.002.
[13] W. Fan, P. Qiao, Vibration-based damage identification methods: a review and comparative study, Struct. Health Monit. 10 (2011) 83–111.
[14] S. Das, P. Saha, S.K. Patro, Vibration-based damage detection techniques used for health monitoring of structures: a review, J. Civ. Struct. Heal. Monit. 6 (2016) 477–507.
[15] M. Radzieński, M. Krawczuk, M. Palacz, Improvement of damage detection methods based on experimental modal parameters, Mech. Syst. Sig. Process. 25 (2011) 2169–2190.
[16] W.-J. Yan, M.-Y. Zhao, Q. Sun, W.-X. Ren, Transmissibility-based system identification for structural health Monitoring: Fundamentals, approaches, and applications, Mech. Syst. Sig. Process. 117 (2019) 453–482.
[17] S. Cantero-Chinchilla, J. Chiachío, M. Chiachío, D. Chronopoulos, A. Jones, A robust Bayesian methodology for damage localization in plate-like structures using ultrasonic guided-waves, Mech. Syst. Sig. Process. 122 (2019) 192–205, https://doi.org/10.1016/j.ymssp.2018.12.021.
[18] S. Ali, D. Thambiratnam, S. Fawzia, K.D. Nguyen, H. Van Den Elsen, I.A. Fujii, Damage detection of an innovative composite slab-girder pedestrian bridge using vibration characteristics, Struct. Infrastruct. Eng. 18 (2022) 807–823.
[19] Y. Liang, D. Li, G. Song, Q. Feng, Frequency co-integration-based damage detection for bridges under the influence of environmental temperature variation, Measurement 125 (2018) 163–175.
[20] S.M.H. Pooya, A. Massumi, A novel and efficient method for damage detection in beam-like structures solely based on damaged structure data and using mode shape curvature estimation, App. Math. Model. 91 (2021) 670–694.
[21] V. Srinivas, K. Ramanjaneyulu, C.A. Jeyasehar, Multi-stage approach for structural damage identification using modal strain energy and evolutionary optimization techniques, Struct. Health Monit. 10 (2011) 219–230.
[22] M. Gul, F.N. Catbas, Statistical pattern recognition for Structural Health Monitoring using time series modeling: theory and experimental verifications, Mech. Syst. Sig. Process. 23 (2009) 2192–2204.
[23] M. Gul, F.N. Catbas, Damage assessment with ambient vibration data using a novel time series analysis methodology, J. Struct. Eng. 137 (2011) 1518–1526.
[24] Y. Goi, C.-W. Kim, Damage detection of a truss bridge utilizing a damage indicator from multivariate autoregressive model, J. Civ. Struct. Heal. Monit. 7 (2017) 153–162.
[25] S. Khan, T. Yairi, A review on the application of deep learning in system health management, Mech. Syst. Sig. Process. 107 (2018) 241–265, https://doi.org/10.1016/j.ymssp.2017.11.024.
[26] C.R. Farrar, K. Worden, Structural health monitoring: a machine learning perspective, 1st ed, Wiley, Chichester, 2013.
[27] N. Mechbal, J.S. Uribe, M. Rébillat, A probabilistic multi-class classifier for structural health monitoring, Mech. Syst. Sig. Process. 60–61 (2015) 106–123, https://doi.org/10.1016/j.ymssp.2015.01.017.
[28] C.K. Oh, H. Sohn, Damage diagnosis under environmental and operational variations using unsupervised support vector machine, J. Sound Vib. 325 (2009) 224–239, https://doi.org/10.1016/j.jsv.2009.03.014.
[29] T. Marwala, Multi-Layer Perceptron for Condition Monitoring in a Mechanical System, in: T. Marwala (Ed.), Condition Monitoring Using Computational Intelligence Methods: Applications in Mechanical and Electrical Systems, Springer, London, 2012: pp. 53–69. https://doi.org/10.1007/978-1-4471-2380-4_3.
[30] X. Yang, C. Fang, P. Kundu, J. Yang, D. Chronopoulos, A decision-level sensor fusion scheme integrating ultrasonic guided wave and vibration measurements for damage identification, Mech. Syst. Sig. Process. 219 (2024) 111597, https://doi.org/10.1016/j.ymssp.2024.111597.
[31] Y. Bao, H. Li, Machine learning paradigm for structural health monitoring, Struct. Health Monit. 20 (2021) 1353–1372, https://doi.org/10.1177/1475921720972416.
[32] E. Figueiredo, G. Park, C.R. Farrar, K. Worden, J. Figueiras, Machine learning algorithms for damage detection under operational and environmental variability, Struct. Health Monit. 10 (2011) 559–572, https://doi.org/10.1177/1475921710388971.
[33] H. Lee, H.J. Lim, T. Skinner, A. Chattopadhyay, A. Hall, Automated fatigue damage detection and classification technique for composite structures using Lamb waves and deep autoencoder, Mech. Syst. Sig. Process. 163 (2022) 108148, https://doi.org/10.1016/j.ymssp.2021.108148.
[34] S. Lawrence, C.L. Giles, A.C. Tsoi, A.D. Back, Face recognition: a convolutional neural-network approach, IEEE Trans. Neural Netw. 8 (1997) 98–113, https://doi.org/10.1109/72.554195.
[35] G. Hu, Y. Yang, D. Yi, J. Kittler, W. Christmas, S.Z. Li, T. Hospedales, When Face Recognition Meets With Deep Learning: An Evaluation of Convolutional Neural Networks for Face Recognition, in: 2015: pp. 142–150.
[36] M. Shahverdy, M. Fathy, R. Berangi, M. Sabokrou, Driver behavior detection and classification using deep convolutional neural networks, Expert Syst. Appl. 149 (2020) 113240, https://doi.org/10.1016/j.eswa.2020.113240.
[37] S. Smeureanu, R.T. Ionescu, M. Popescu, B. Alexe, Deep appearance features for abnormal behavior detection in video, in: S. Battiato, G. Gallo, R. Schettini, F. Stanco (Eds.), Image Analysis and Processing - ICIAP 2017, Springer International Publishing, Cham, 2017, pp. 779–789.
[38] K. Sohn, D.Y. Jung, H. Lee, A.O. Hero, Efficient learning of sparse, distributed, convolutional feature representations for object recognition, IEEE, 2011, pp. 2643–2650.
[39] L. Shang, Q. Yang, J. Wang, S. Li, W. Lei, Detection of rail surface defects based on CNN image recognition and classification, IEEE, 2018, pp. 45–51.
[40] A. Litvintseva, O. Evstafev, S. Shavetov, Real-time steel surface defect recognition based on CNN, IEEE, 2021, pp. 1118–1123.
[41] F. Wei, G. Yao, Y. Yang, Y. Sun, Instance-level recognition and quantification for concrete surface bughole based on deep learning, Autom. Constr. 107 (2019) 102920.
[42] Y.-J. Cha, W. Choi, O. Büyüköztürk, Deep learning-based crack damage detection using convolutional neural networks, Comput. Aided Civ. Inf. Eng. 32 (2017) 361–378.
[43] O. Abdeljaber, O. Avci, S. Kiranyaz, M. Gabbouj, D.J. Inman, Real-time vibration-based structural damage detection using one-dimensional convolutional neural networks, J. Sound Vib. 388 (2017) 154–170.
[44] O. Avci, O. Abdeljaber, S. Kiranyaz, M. Hussein, D.J. Inman, Wireless and real-time structural damage detection: A novel decentralized method for wireless sensor networks, J. Sound Vib. 424 (2018) 158–172, https://doi.org/10.1016/j.jsv.2018.03.008.

[45] O. Abdeljaber, O. Avci, M.S. Kiranyaz, B. Boashash, H. Sodano, D.J. Inman, 1-D CNNs for structural damage detection: Verification on a structural health monitoring benchmark data, Neurocomputing 275 (2018) 1308–1317.
[46] Y. Zhou, Y. Zheng, Y. Liu, T. Pan, Y. Zhou, A hybrid methodology for structure damage detection uniting FEM and 1D-CNNs: demonstration on typical high-pile wharf, Mech. Syst. Sig. Process. 168 (2022) 108738.
[47] S. Yang, Y. Huang, Damage identification method of prestressed concrete beam bridge based on convolutional neural network, Neural Comput. Appl. 33 (2021) 535–545.
[48] Y. Sarawgi, S. Somani, A. Chhabra, Nonparametric vibration based damage detection technique for structural health monitoring using 1D CNN, Springer, 2019, pp. 146–157.
[49] S. Sharma, S. Sen, One-dimensional convolutional neural network-based damage detection in structural joints, J. Civ. Struct. Heal. Monit. 10 (2020) 1057–1072.
[50] S. Li, M. Cao, M. Bayat, D. Sumarac, J. Wang, An intelligent framework of upgraded CapsNets with massive transmissibility data for identifying damage in bridges, Appl. Soft Comput. 155 (2024) 111459, https://doi.org/10.1016/j.asoc.2024.111459.
[51] Y.-J. Cha, R. Ali, J. Lewis, O. Büyüköztürk, Deep learning-based structural health monitoring, Autom. Constr. 161 (2024) 105328, https://doi.org/10.1016/j.autcon.2024.105328.
[52] S. Teng, X. Chen, G. Chen, L. Cheng, D. Bassir, Structural damage detection based on convolutional neural networks and population of bridges, Measurement 202 (2022) 111747, https://doi.org/10.1016/j.measurement.2022.111747.
[53] Z.-D. Li, W.-Y. He, W.-X. Ren, Structural damage identification based on Wasserstein Generative Adversarial Network with gradient penalty and dynamic adversarial adaptation network, Mech. Syst. Sig. Process. 221 (2024) 111754, https://doi.org/10.1016/j.ymssp.2024.111754.
[54] Z.-D. Li, W.-Y. He, W.-X. Ren, Y.-L. Li, Y.-F. Li, H.-C. Cheng, Damage detection of bridges subjected to moving load based on domain-adversarial neural network considering measurement and model error, Eng. Struct. 293 (2023) 116601, https://doi.org/10.1016/j.engstruct.2023.116601.
[55] A. Fernandez-Navamuel, D. Pardo, F. Magalhães, D. Zamora-Sánchez, Á.J. Omella, D. Garcia-Sanchez, Bridge damage identification under varying environmental and operational conditions combining Deep Learning and numerical simulations, Mech. Syst. Sig. Process. 200 (2023) 110471, https://doi.org/10.1016/j.ymssp.2023.110471.
[56] R. Doroudi, S.H.H. Lavassani, M. Shahrouzi, Optimal tuning of three deep learning methods with signal processing and anomaly detection for multi-class damage detection of a large-scale bridge, 14759217231216694, Struct. Health Monit. (2024), https://doi.org/10.1177/14759217231216694.
[57] S. Das, P. Saha, Structural health monitoring techniques implemented on IASC–ASCE benchmark problem: a review, J. Civ. Struct. Heal. Monit. 8 (2018) 689–718.
[58] T. Liu, H. Xu, M. Ragulskis, M. Cao, W. Ostachowicz, A data-driven damage identification framework based on transmissibility function datasets and one-dimensional convolutional neural networks: Verification on a structural health monitoring benchmark structure, Sensors 20 (2020) 1059.
[59] X. Bao, T. Fan, C. Shi, G. Yang, One-dimensional convolutional neural network for damage detection of jacket-type offshore platforms, Ocean Eng. 219 (2021) 108293.
[60] G. Zhang, Y. Ge, Vibration characteristics test and analysis on concrete box girder continuous pedestrian bridge, J. Vibr. Shock 28 (2009), 102–106+204.
[61] L. Sun, W. Xie, Experimental assessment of soil–structure interaction effects on a super long-span cable-stayed-bridge with pile group foundations, Bull. Earthq. Eng. 17 (2019) 3169–3196.
[62] B. Han, S. Chen, J. Liang, Influence of Structure-Soil-Structure Dynamic Interaction on Structural System Frequencies, J. Earthq. Eng. 41 (2019) 1574–1580.
[63] L. Sun, Z. Shang, Y. Xia, Development and prospect of bridge structural health monitoring in the context of big data, China J. Highway Transport. 32 (2019) 1–20.
[64] I. Goodfellow, J. Pouget-Abadie, M. Mirza, B. Xu, D. Warde-Farley, S. Ozair, A. Courville, Y. Bengio, Generative Adversarial Nets, in: Z. Ghahramani, M. Welling, C. Cortes, N. Lawrence, K.Q. Weinberger (Eds.), Advances in Neural Information Processing Systems, Curran Associates, Inc., 2014.
[65] I. Goodfellow, J. Pouget-Abadie, M. Mirza, B. Xu, D. Warde-Farley, S. Ozair, A. Courville, Y. Bengio, Generative adversarial networks, Commun. ACM 63 (2020) 139–144, https://doi.org/10.1145/3422622.
[66] H. Fathnejat, B. Ahmadi-Nedushan, S. Hosseininejad, M. Noori, W.A. Altabey, A data-driven structural damage identification approach using deep convolutional-attention-recurrent neural architecture under temperature variations, Eng. Struct. 276 (2023) 115311, https://doi.org/10.1016/j.engstruct.2022.115311.
[67] H. Wan, L. Gao, M. Su, Q. Sun, L. Huang, Attention-based convolutional neural network for pavement crack detection, Adv. Mater. Sci. Eng. 2021 (2021) 5520515, https://doi.org/10.1155/2021/5520515.
[68] K.A. Eltouny, X. Liang, Large-scale structural health monitoring using composite recurrent neural networks and grid environments, Comput. Aided Civ. Inf. Eng. 38 (2023) 271–287, https://doi.org/10.1111/mice.12845.
[69] P. Balasubramanian, V. Kaushik, S.Y. Altamimi, M. Amabili, M. Alteneiji, Comparison of neural networks based on accuracy and robustness in identifying impact location for structural health monitoring applications, Struct. Health Monit. 22 (2023) 417–432, https://doi.org/10.1177/14759217221098569.
[70] M. Azimi, T.Y. Yang, Transformer-based framework for accurate segmentation of high-resolution images in structural health monitoring, Comput.-Aided Civ. Infrastruct. Eng. n/a (n.d.). https://doi.org/10.1111/mice.13211.
[71] H. Triviño, C. Feijóo, H. Lugmania, Y. Vidal, C. Tutivén, Damage detection and localization at the jacket support of an offshore wind turbine using transformer models, Struct. Control Health Monit. 2023 (2023) 6646599, https://doi.org/10.1155/2023/6646599.
[72] A. Entezami, H. Shariatmadar, An unsupervised learning approach by novel damage indices in structural health monitoring for damage localization and quantification, Struct. Health Monit. 17 (2018) 325–345, https://doi.org/10.1177/1475921717693572.
[73] A. Entezami, H. Sarmadi, B. Behkamal, C. De Michele, On continuous health monitoring of bridges under serious environmental variability by an innovative multi-task unsupervised learning method, Struct. Infrastruct. Eng. (2023) 1–19, https://doi.org/10.1080/15732479.2023.2166538.
[74] A. Peryanto, A. Yudhana, R. Umar, Klasifikasi Citra Menggunakan convolutional neural network dan K Fold cross validation, J. Appl. Inform. Comput. 4 (2020) 45–51, https://doi.org/10.30871/jaic.v4i1.2017.